JOURNAL OF MATERIALS SCIENCE **39** (2004) 6655–6673

Imaging and microanalysis of liquid phase sintered silicon-based ceramic microstructures

L. K. L. FALK
Department of Experimental Physics, Chalmers University of Technology, SE-412 96 Göteborg, Sweden
E-mail: lklfalk@fy.chalmers.se

This review paper is focussed on the characterization of the microstructural development during liquid phase sintering and post-densification crystallisation heat treatment of ceramic materials based on the Si_3N_4 or SiC structures. Grain shape and size distributions, assessed by quantitative microscopy in combination with stereological methods, and fine scale microstructures, investigated by electron diffraction and high resolution imaging and microanalysis in the TEM, are discussed and related to the fabrication process and the overall composition of the ceramic material. It is demonstrated that combined high resolution analytical and spatial information from chemically and structurally distinct fine scale features, such as grain boundary films of residual glass, is obtained by electron spectroscopic imaging and subsequent computation of elemental distribution images. These images reveal that residual glassy grain boundary films are rich in oxygen and cations originating from the metal oxide/nitride additives, consistent with fine probe EDX analysis in the FEGTEM. Elemental analysis with high spatial resolution has also shown that grain growth into pockets of residual liquid/glass is associated with diffusion profiles in the glass in front of the growing grain. High resolution imaging in the TEM and elemental maps computed from electron energy filtered images show that the intergranular film thickness, in general, varies within a particular silicon nitride or sialon microstructure. Furthermore, grain boundaries, apparently free from residual glass may co-exist with glass-containing grain boundaries in some silicon nitride microstructures. In addition to the choice and weight fraction of sintering additives, factors such as the ionic radius of the cations originating from the additives, the local nano-scale chemistry and the relative grain orientation have an effect on the volume fraction and morphology of the intergranular microstructure.

1. Introduction

The Si_3N_4 and SiC structures contain small and comparatively closely packed atoms. The interatomic bonding in these structures is strongly covalent, which, together with the atomic arrangement, gives a large number of strong bonds per unit volume. This results in a combination of good inherent mechanical and chemical properties such as a high strength, a high value of Young's modulus, good oxidation and corrosion resistance and a low thermal expansion coefficient. Ceramic materials based on the Si_3N_4 or SiC structures are, consequently, potential high strength materials for structural applications at both high and ambient temperatures [1–7].

The strong interatomic bonding results also in extremely low self-diffusivities at temperatures below that where appreciable decomposition of the ceramic compound starts. The fabrication of dense SiC and Si_3N_4-based materials requires, therefore, a sintering additive that promotes densification, and at the same time inhibits the decomposition of the ceramic compound [1–4, 7–11].

The sintering additives will, however, in general introduce an intergranular microstructure that may limit the performance of the material [1–7, 12–18]. Refractory secondary phases and a strong intergranular bonding are required for high strength and creep resistance at elevated temperatures. The activation of different toughening mechanisms such as crack deflection and bridging, and micro-cracking rely, on the other hand, on "sufficiently weak" interfaces. It becomes, hence, important to control the intergranular microstructure, in addition to the grain morphology and composition.

This review is concerned with the development of microstructure in two classes of liquid phase sintered silicon-based ceramics: Si_3N_4/sialon ceramics and α-SiC ceramics. The use of scanning and transmission electron microscopy (SEM and TEM) in the characterisation of the ceramic microstructures will be illustrated, and particular attention will be given to high resolution

imaging and microanalysis of intergranular structures in the TEM.

2. Liquid phase sintering

Liquid phase sintering of ceramic materials based on the Si_3N_4 or SiC structures requires the addition of metal oxides or nitrides [1–4, 7, 9, 19, 20]. Above relevant eutectic temperatures, the sintering additives react with the inherent surface silica present on the starting powder particles to form a liquid phase that serves as a mass transport medium and, hence, promotes densification. Some of the Si_3N_4 or SiC may also participate in the formation of the liquid phase sintering medium, and this will, in most cases, lower the eutectic temperatures of these systems [19, 21]. The chemistry and the volume fraction of the liquid is determined by the choice of additives and also by densification parameters such as the atmosphere and the temperature/time programme during sintering. The kinetics of the densification process may be described by the three stages of Kingery's model for liquid phase sintering: particle rearrangement in the liquid phase, a solution/reprecipitation process of the solid phase, and final coalescence [19, 22]. The properties of the liquid phase sintering medium will determine the densification rate and the extent of grain growth, and thereby the grain shape and size distribution of the sintered material [14, 23, 24].

The final microstructure of the liquid phase sintered ceramic consists of grains of Si_3N_4/sialon, or SiC, and, in general, also intergranular phases, see Figs 1–3. Secondary crystalline phases may partition from the liquid phase sintering medium, but a certain volume fraction of the liquid is generally retained as a residual glass in the microstructure of the sintered ceramic.

It has been demonstrated that Si_3N_4 powder compacts without additives may be fully densified by hot isostatic pressing (HIP); the inherent surface silica layer present on the Si_3N_4 powder particles provides a sufficient sintering additive in combination with the applied high pressure [25]. This results in a Si_3N_4 ceramic with a minimum of residual grain boundary glass, see Fig. 4a. HIP of SiC powder compacts containing only smaller additions of metal oxides ($\leq$3 wt% of Al_2O_3 and/or Y_2O_3) is, on the other hand, accompanied by a limited decomposition of the SiC according to the reaction

$$SiC + 2/3M_2O_3 \rightarrow SiO_2 + 4/3M + C(\text{graphite}) \quad (1)$$

where M stands for Al and/or Y [20]. This decomposition results in the formation of intergranular graphite as shown in Fig. 4b.

Impurities that originate from the starting powders, or are introduced during the preparation of green bodies, will, generally, lower the eutectic temperature and concentrate to the liquid phase sintering medium. As a consequence, most impurities will, eventually, be part of the intergranular microstructure. This may have a detrimental effect on the high temperature properties of the ceramic because of the less refractory nature of impurity containing glass and secondary phases.

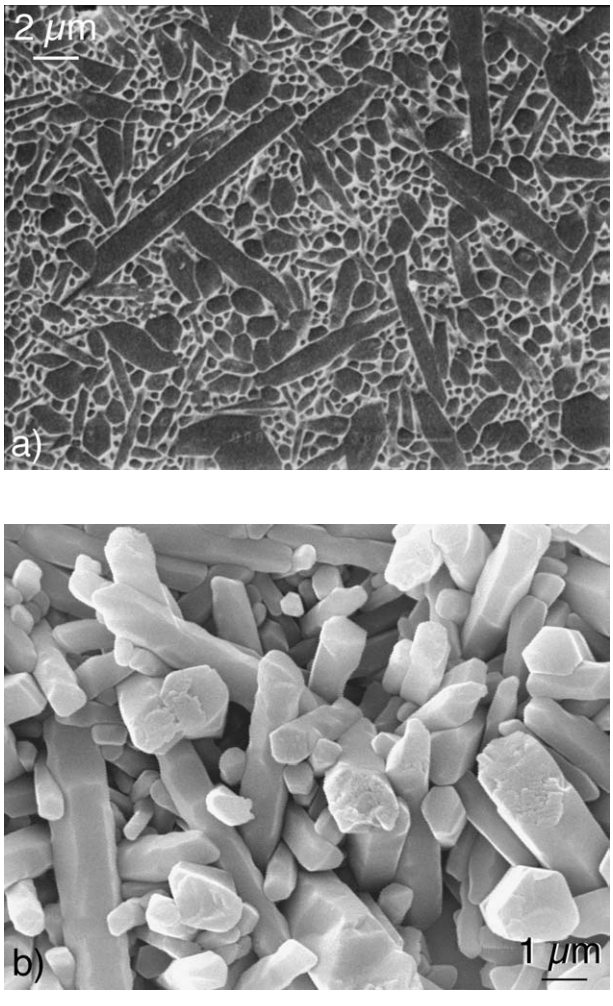

Figure 1 The microstructure of a silicon nitride material fabricated with the addition of 9 wt% Y_2O_3 and Al_2O_3 with a molar ratio corresponding to that of the Y,Al-garnet (YAG), $5Al_2O_3{\cdot}3Y_2O_3$. (a) Plasma etched section displaying β'-Si_3N_4 grain sections separated by an intergranular microstructure that appears with bright contrast (SEM). (b) Section subjected to excessive chemical etching, which reveals the prismatic shape of the elongated β'-Si_3N_4 grains (SEM).

3. Silicon nitride and sialon ceramics

The compound Si_3N_4 occurs with two different crystal structures, α- and β-Si_3N_4. α-Si_3N_4 has a trigonal crystal structure (space group P31c), but is often indexed according to a hexagonal unit cell with $a = 0.7765$ nm and $c = 0.5618$ nm [26]. β-Si_3N_4 is hexagonal (space group $P6_3/m$) with lattice parameters $a = 0.7608$ nm and $c = 0.2911$ nm [26, 27]. Both the α- and β-Si_3N_4 structures are built up by a three-dimensional network of corner sharing SiN_4 tetrahedra, and each nitrogen atom is shared by three tetrahedra [28]. The idealised structures may be described as a stacking of Si and N containing layers in an ABCDABCD. . . and an ABAB. . . sequence for the α and β modifications, respectively [28]. This stacking results in long channels parallel to the c-axis in the β-Si_3N_4 structure. A c-glide plane relates the CD layers to the AB layers in the α structure, and this results in large closed interstitial sites in α-Si_3N_4.

Liquid phase sintering of powder compacts containing both the α- and β-Si_3N_4 structures involves a transformation of the α structure to β-Si_3N_4. This transformation is reconstructive; the α-Si_3N_4 is

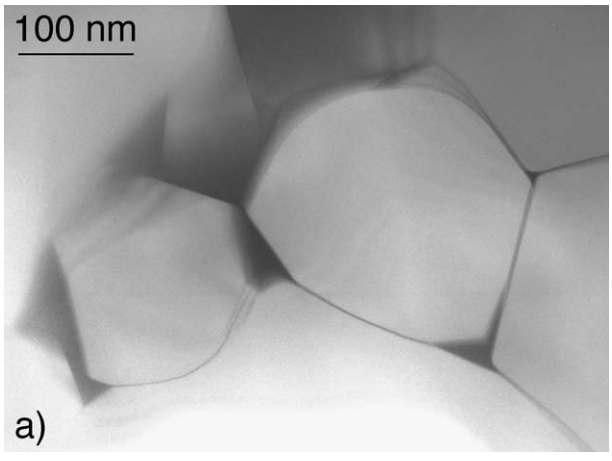

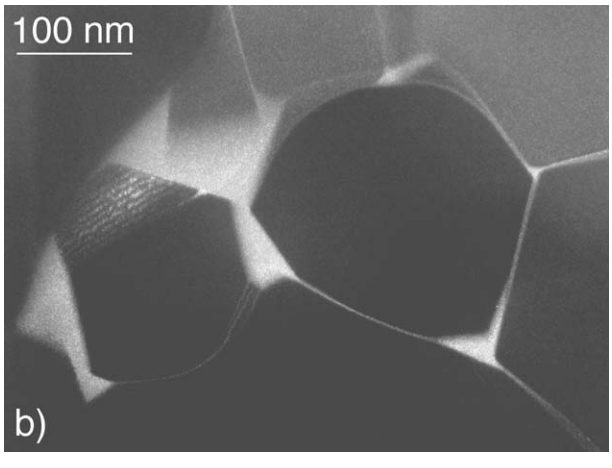

Figure 2 β'-Si_3N_4 grains in a duplex α/β sialon microstructure. The β' grains are surrounded by a residual glass that appears with dark contrast in the TEM bright field image in (a) because of its neodymium content. The substitution levels of the β' grains correspond to z-values of 0.4 and 0.5 as determined from EDX point ananlysis in the TEM. The intergranular glass is imaged in dark field in (b).

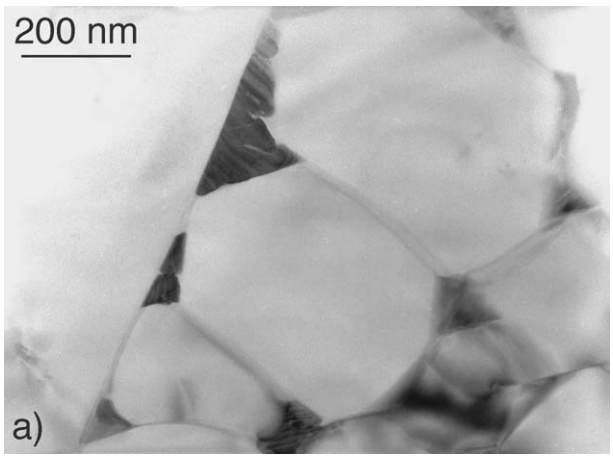

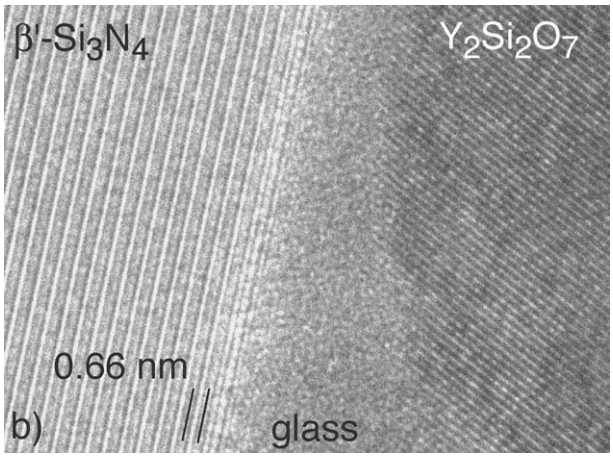

Figure 3 The silicon nitride based microstructure of a material fabricated with additions of Y_2O_3 and Al_2O_3 (TEM). Faceted β'-Si_3N_4 grain sections are separated by a partly crystallised intergranular microstructure (a). The secondary crystalline phase is separated from the β' grains by residual glass as shown in (b).

preferentially dissolved in the liquid phase sintering medium, and grains of β-Si_3N_4 precipitate and grow from the liquid [2, 19]. The mass transport associated with this solution/precipitation process contributes to the densification of the powder compact.

A high density Si_3N_4 material may, however, be obtained with only a limited transformation of α- to β-Si_3N_4 [14, 17, 29]. The application of a high pressure during consolidation, e.g. as in HIP, promotes densification, and full density may be achieved before the α- to β-Si_3N_4 transformation is complete and equilibrium has been attained [14, 17]. This has been observed for Si_3N_4 ceramics fabricated with up to 20 wt% sintering additives.

Virtually fully dense Si_3N_4-based ceramics may be obtained without any significant contribution from the α- to β-Si_3N_4 transformation also during pressureless sintering of compacts containing larger amounts of oxide additives [29]. A temperature/time programme for pressureless sintering of Si_3N_4 composite ceramics fabricated with the addition of 30 wt% ZrO_2(+3 mol% Y_2O_3) and 5 wt% Al_2O_3 is shown in Fig. 5a together with the phase composition of partially sintered powder compacts. Liquid phase formation at temperatures in the range 1350 to 1650°C resulted in a virtually fully dense material during heating to the final sintering temperature. This density increase was associated with only a limited transformation of the α- to β-Si_3N_4, and particle rearrangement in the liquid phase made, hence, the major contribution to densification. Prolonged holding at 1650°C resulted in an accelerated dissolution of α-Si_3N_4 in the liquid, and a β-Si_3N_4/Si_2N_2O/ZrO_2 microstructure, with only a limited fraction of residual glass, developed, see Fig. 5b and c.

The sialon systems have a potential for the fabrication of Si_3N_4-based ceramics with a minimum of residual glass through the incorporation of elements originating from the sintering additives into grains of α- and/or β-sialon and other, secondary, crystalline phases [30]. The α- and β-sialons are solid solutions based on the α- and β-Si_3N_4 structures [4, 27, 31]. α-sialon (α'-Si_3N_4) has a composition given by $R_xSi_{12-(m+n)}Al_{m+n}O_nN_{16-n}$, where m(Si-N) are substituted by m(Al-N), and n(Si-N) by n(Al-O) in the α-Si_3N_4 structure. The valence discrepancy introduced by this substitution is compensated for by the interstitial cation R^{p+}, and $x = m/p$. Cations such as Y^{3+}, Yb^{3+}, Dy^{3+}, Sm^{3+} and Nd^{3+} are well known to stabilize the α' structure. The corresponding oxides, as well as Al_2O_3, are recognized as efficient liquid phase sintering additives to silicon nitride. β-sialon (β'-Si_3N_4) forms when Si in the β-Si_3N_4 structure is substituted by aluminum, and some

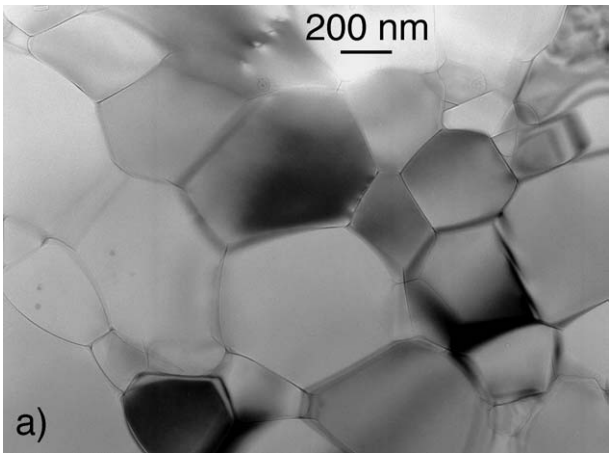

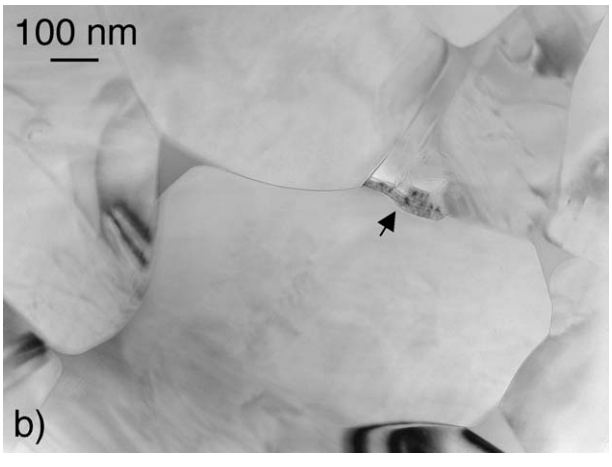

Figure 4 (a) The microstructure of a Si_3N_4 ceramic fabricated by HIP without the addition of sintering aids. (b) Graphite formation (arrowed) in a SiC ceramic HIP:ed with the addition of 1.3 wt% Al_2O_3 and 1.7 wt% Y_2O_3.

nitrogen at the same time is replaced by oxygen for the retention of charge neutrality. The general formula of β-sialon is $Si_{6-z}Al_zO_zN_{8-z}$, where $z \leq 4.2$. In addition, the α- and β-sialon structures allow the development of self-reinforced, duplex, microstructures consisting of fibrous β' grains in a harder α' matrix [32, 33].

4. Imaging and analysis

4.1. Grain size and shape

The overall ceramic microstructure may be described by two-dimensional grain section parameter distributions determined by quantitative microscopy of polished and etched sections through the microstructure, see Fig. 1a. These observations do not, however, provide an accurate information about the real three-dimensional grain shape and grain size distribution. An hypothesis on grain shape is required in order to relate the experimentally determined two-dimensional grain section parameter distributions to the true three-dimensional microstructure of the material [34–36]. As demonstrated by Wasén and Warren [35–37], computer-generated sections and linear intercepts of bodies with selected shapes will provide stereological parameters that can be used both to identify an *average* grain shape from two-dimensional measure-

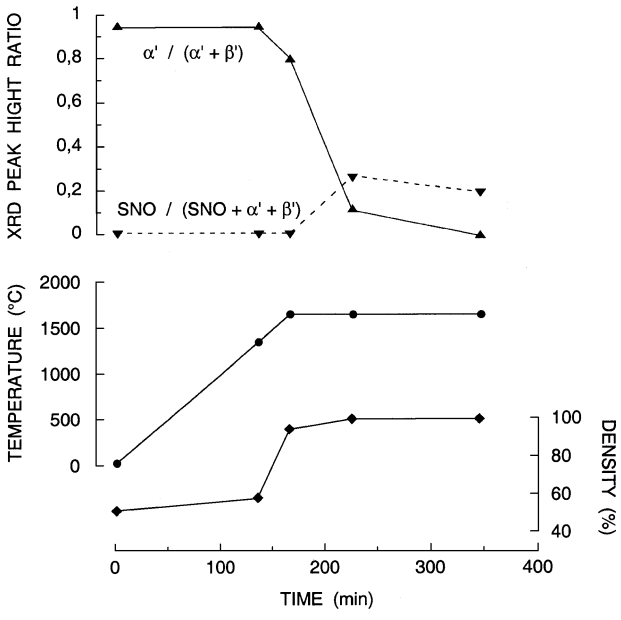

(a)

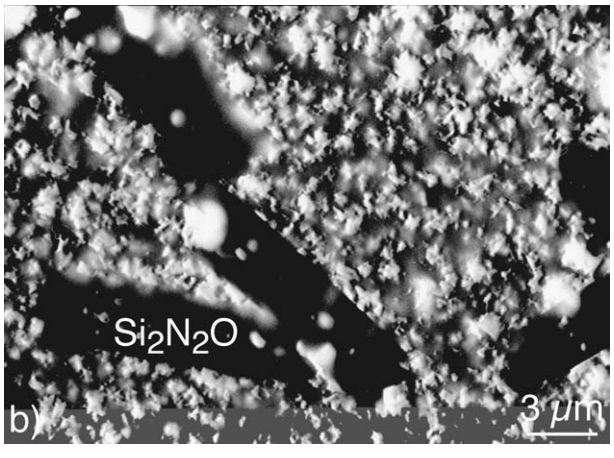

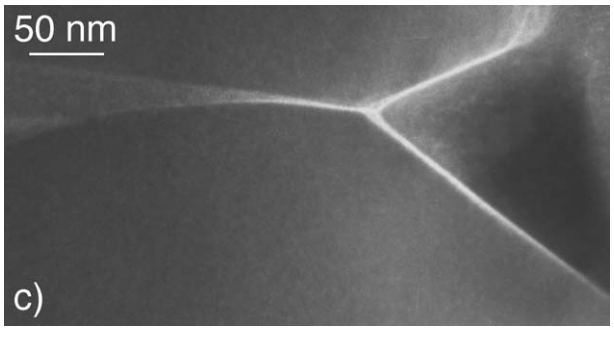

Figure 5 (a) The temperature/time programme for pressureless sintering of composite Si_3N_4 + 30 wt% ZrO_2(+3 mol% Y_2O_3) ceramics and the density and phase composition of compacts from different stages in the fabrication process (α', $\beta' = \alpha'$-, β'-Si_3N_4; SNO = Si_2N_2O). (b) The microstructure after 3 h at the sintering temperature 1650°C. The ZrO_2 grains appear with white contrast in this SEM image formed with back-scattered electrons. (c) The residual glass is concentrated to very thin grain boundary films (TEM centered dark field image formed from diffuse scattered electrons).

ments on a section, and as the basis for a *reconstruction* of the three-dimensional grain size distribution. Once the average grain shape has been established, computer generated section parameter distributions for this shape can be used in a determination of the three-dimensional grain size distribution as described in references [36–38]. The application of this method for the assessment

of three-dimensional grain size distributions in Si_3N_4 microstructures is described in more detail in Section 5 below.

4.2. Imaging of residual glass and grain boundary structure

Larger volumes of residual glass, such as pockets at multi-grain junctions, are readily identified in the TEM because of their lack of diffraction contrast when the thin foil specimen is tilted under the electron beam. This technique is, however, not applicable when the glassy phase is present as thin grain boundary films. Grain boundary structures and intergranular films are, instead, directly, or indirectly, identified and imaged by different, well established, techniques in the TEM [39–43].

4.2.1. Diffuse dark field imaging

Dark field images formed from part of the diffuse scattering from the glass are direct images of the distribution of the intergranular glass, see Figs 2 and 6a. The incident electron beam is deflected off the optic axis, and a portion of the halo formed by the diffuse scattered electrons from the amorphous material is centered, and selected by the objective aperture. The glassy areas will appear with bright contrast in these images, and it is essential to minimize the contribution from Bragg diffracted electrons from the surrounding grains in order to obtain good image contrast.

Thickness measurements of edge-on grain boundary films imaged in dark field will, in general, give an overestimate of film thickness [41]. The scattering of the incident electron beam will be affected by artefacts introduced during specimen preparation, e.g., grain boundary grooving and re-deposition of sputtered matter during ion beam milling, as well as by the presence of an evaporated carbon film on a thin foil of a non-conducting ceramic material. Specimen drift may be one other experimental error because of the need for long exposure times at high magnifications.

4.2.2. Defocus Fresnel imaging

Defocus Fresnel images show contrast around areas where the mean inner potential changes abruptly [42]. The contrast in these images depends on defocus, and is lost when the specimen is imaged at Gaussian focus, see Figs 6 and 7. Defocus Fresnel imaging may be used as an indirect technique for the determination of grain boundary film thickness, see Fig. 7b. An underfocussed image of a grain boundary containing a film shows a pair of dark lines (fringes) delineating the boundary. This contrast is reversed when going through Gaussian focus so that an overfocussed image contains a pair of bright lines. If the boundary is imaged in a TEM equipped with a field emission gun (FEG), higher order Fresnel fringes with weaker contrast may also be visible because of the high coherency of the FEG. There is reflection symmetry in the fringe contrast when the grain boundary is oriented edge-on, and this may be used as a general aid in grain boundary orientation.

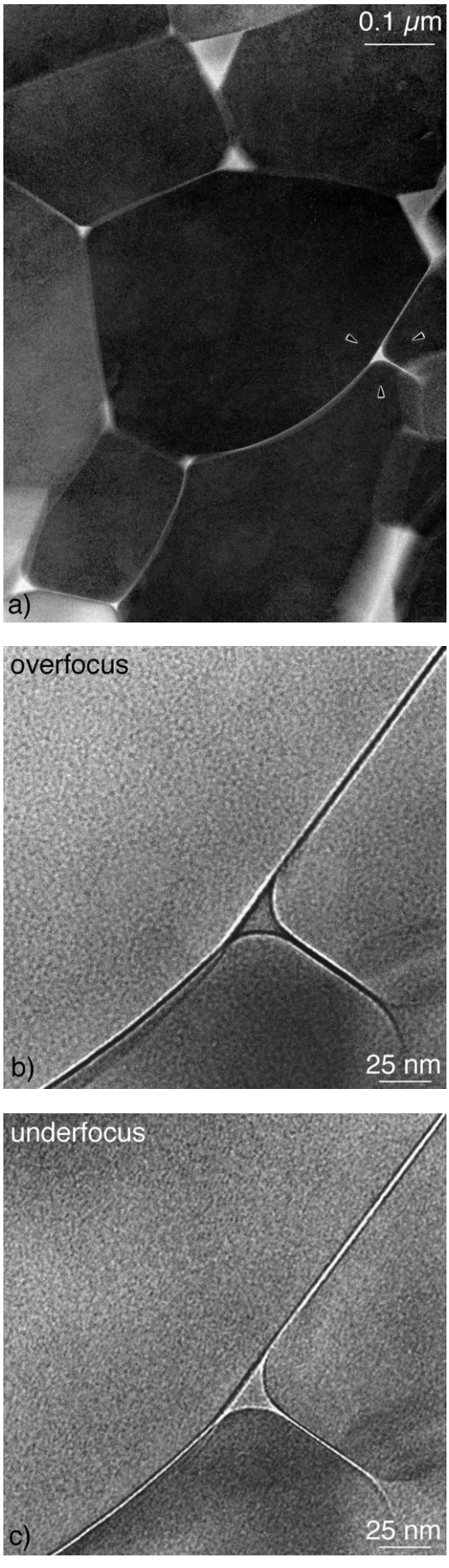

Figure 6 The residual intergranular glassy phase in a silicon nitride ceramic. The TEM centered dark field image in (a) shows that the glass is present as thin intergranular films merging into pockets at multi-grain junctions. Over- and underfocus Fresnel images of the triple-grain junction arrowed in (a) are shown in (b) and (c), respectively.

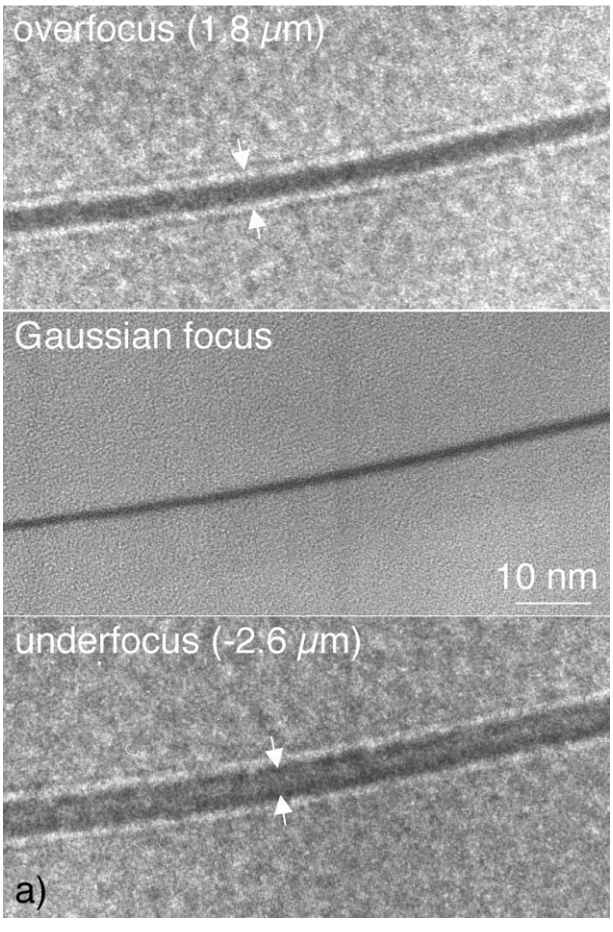

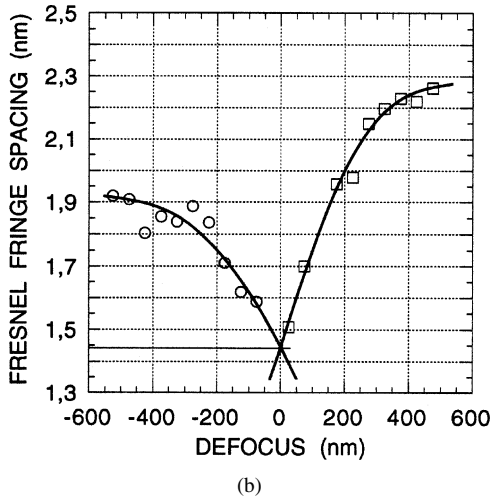

(b)

Figure 7 (a) Defocus Fresnel images of a grain boundary in an α-sialon ceramic fabricated with the addition of Dy_2O_3. Segregation of dysprosium to the glassy grain boundary film results in the absorption contrast in the image taken close to Gaussian focus. First order maxima (overfocus) and minima (underfocus) are arrowed. Higher order Fresnel fringes are also visible in the over- and underfocus images because of the high coherency of the electron beam produced in the FEGTEM. (b) Fresnel fringe spacing as function of defocus in over- and underfocussed images of a SiC/SiC grain boundary in an α-SiC ceramic pressureless sintered with Y_2O_3 and Al_2O_3. The film thickness was estimated to 1.4–1.5 nm.

The separation between the first fringe maximum, or minimum, intensity in an image of an edge-on grain boundary depends on the film thickness and the defocus [41, 42]. The film thickness may, hence, be estimated from plots of fringe spacing as function of defocus; the intersection of plots of overfocus and underfocus series extrapolated to zero defocus represents the grain boundary film thickness, see Fig. 7b. There are, however, different experimental uncertainties associated with defocus Fresnel imaging of grain boundary films. The fringe visibility is strongly affected by the diffraction conditions in the grains on either side of the boundary film; a weakly diffracting grain will promote fringe contrast and thereby a more accurate measurement of fringe spacing. Drift of focus and image during recording of through focus series with a large number of images will have a strong effect on the estimated film thickness.

4.2.3. High resolution lattice imaging

High resolution lattice imaging makes it possible to image grain boundary detail with the resolution of an interplanar spacing in the crystal structures of the neighbouring grains, see Fig. 8. This technique will give a direct and accurate image of the grain boundary region when the grain boundary is in an edge-on orientation, and the adjacent grains in good diffracting conditions so that interference fringes are produced on either side

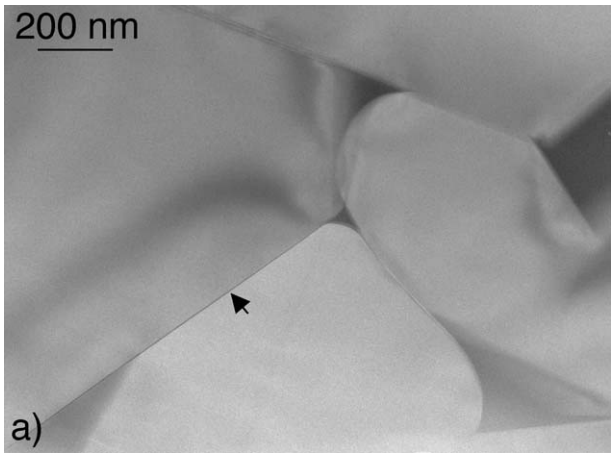

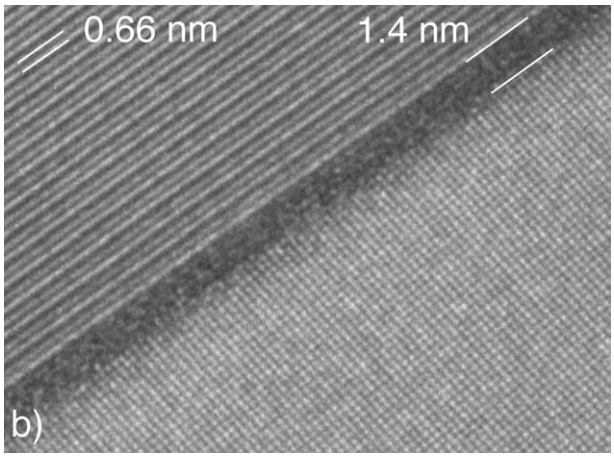

Figure 8 The residual intergranular glassy phase in a silicon nitride ceramic gas pressure sintered at 1950 °C with the addition of 3 wt% Y_2O_3. The grain boundary region arrowed in (a) is imaged in high resolution in (b). The discontinuity in the lattice fringes at the interface between the two grains corrrespond to a film thickness of 1.4 nm. The glass, including the amorphous grain boundary films, contained yttrium and oxygen originating from thte sintering additive, and also some impurity calcium.

of the film. Imaging is carried out with the incident electron beam on-axis, and ± **g** are allowed through the objective aperture together with the direct beam. If the specimen is sufficiently thin, the grains will have a sinusodial image contrast with a fringe spacing corresponding to the interplanar spacing giving rise to the reciprocal lattice vector **g**.

The lattice fringes are, however, not localized [43, 44]. Images should, therefore, be recorded at different defoci close to Scherzer and zero defocus; a different defocus may cause the two sets of fringes to extend into the gap and obscure the grain boundary film. This fringe shift with defocus is an electron optical effect that is microscope dependent. Provided that an image is recorded at a proper defocus, the area of discontinuity in the lattice fringes at the interface between two neighbouring grains will correspond to the thickness of the intergranular film. The grain boundary film thickness may, then, be determined from the spacing of the lattice fringes in the grains.

4.3. Chemical analysis and electron spectroscopic imaging

The incident electrons may be inelastically scattered, which is associated with a certain loss in electron energy, on their way through the thin-foil TEM specimen [45]. Inelastic scattering processes involving the excitation of inner shell electrons are accompanied by the emission of characteristic X-rays. A correlation of chemical information to the fine scale structure may, hence, be obtained by energy dispersive X-ray (EDX) analysis or electron energy loss spectroscopy (EELS) when a focussed probe is stepped across the thin foil specimen in the TEM.

High resolution chemical information may also be obtained from electron spectroscopic imaging, also referred to as energy filtered TEM [39, 46–49]. These images combine two-dimensional spatial and elemental information, and are produced by an energy filter that separates the contribution from electrons with different energies. It becomes, then, possible to select certain electron energies for imaging by placing an energy selecting slit in a plane containing a focussed EEL spectrum.

4.3.1. The energy of transmitted electrons

The zero loss peak is the most intense feature in the energy spectrum of the transmitted electrons, see Fig. 9a. This peak contains mainly the unscattered and the elastically scattered electrons, and is followed by the plasmon peak which contains electrons that have suffered energy losses arising from interactions with weakly bond electrons. The EEL spectrum above the plasmon peak consists of element characteristic edges superimposed on a background that is rapidly decreasing towards higher energy losses, see Fig. 9.

In zero loss imaging and diffraction, the unscattered and elastically scattered electrons are selected by the slit in the energy filter [46, 47]. This improves the contrast

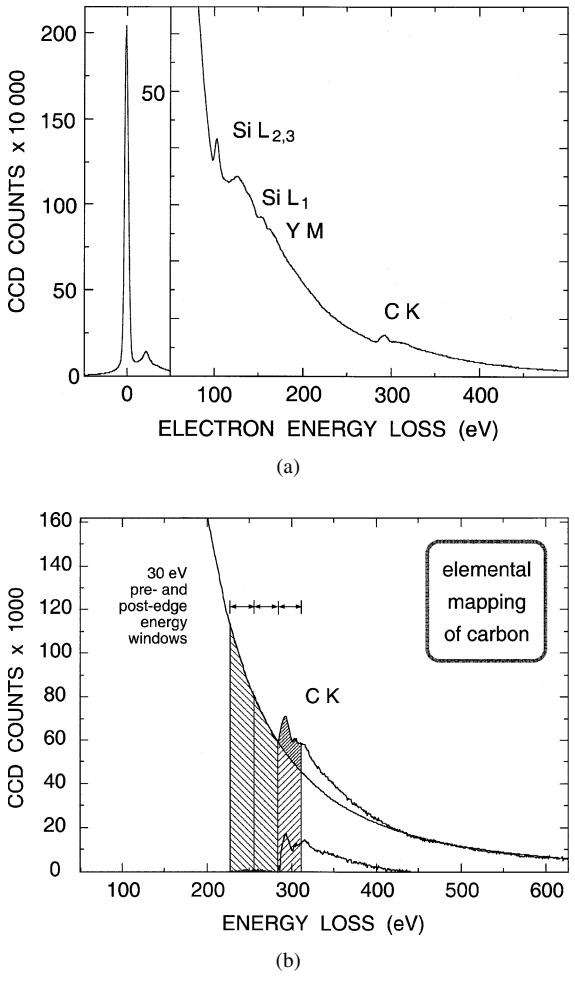

Figure 9 (a) EEL spectrum from an α-SiC ceramic HIP:ed with the addition of Y_2O_3. (b) Selection of energy losses for image acquisition around the C K edge.

of the image, or the diffraction pattern, because the inelastically scattered electrons that are defocused due to the chromatic aberration of the objective lens are filtered away.

The correlation of chemical information to structure is shown in elemental distribution images computed from electron spectroscopic images recorded around the element specific edges in the EEL spectrum. The technique allows the extraction of analytical and spatial information from regions with a size down to 1 to 2 nm [39]. It has also been demonstrated that phase contrast may be preserved in electron energy filtered images and computed elemental distribution images [39, 46, 50]. This allows an accurate size determination of chemically distinct fine scale features such as the thickness of grain boundary films.

4.3.2. Elemental distribution images

Two types of elemental distribution images can be obtained from electron energy filtered images: elemental maps and jump ratio maps [47]. An elemental map is computed by subtracting a background image from a post-edge image containing the element specific signal. The background image is calculated from two pre-edge images according to a suitable mathematical model, e.g., the power-law model, for extrapolating EEL

spectral background under an element specific edge. The power-law model gives the background intensity in the post-edge image as

$$I = AE^{-r} \quad (3)$$

where E is the energy loss and the A and r parameters are calculated pixel by pixel from the two pre-edge images [47]. The computation of a carbon elemental map from electron energy filtered images is shown in Figs 9b and 10a.

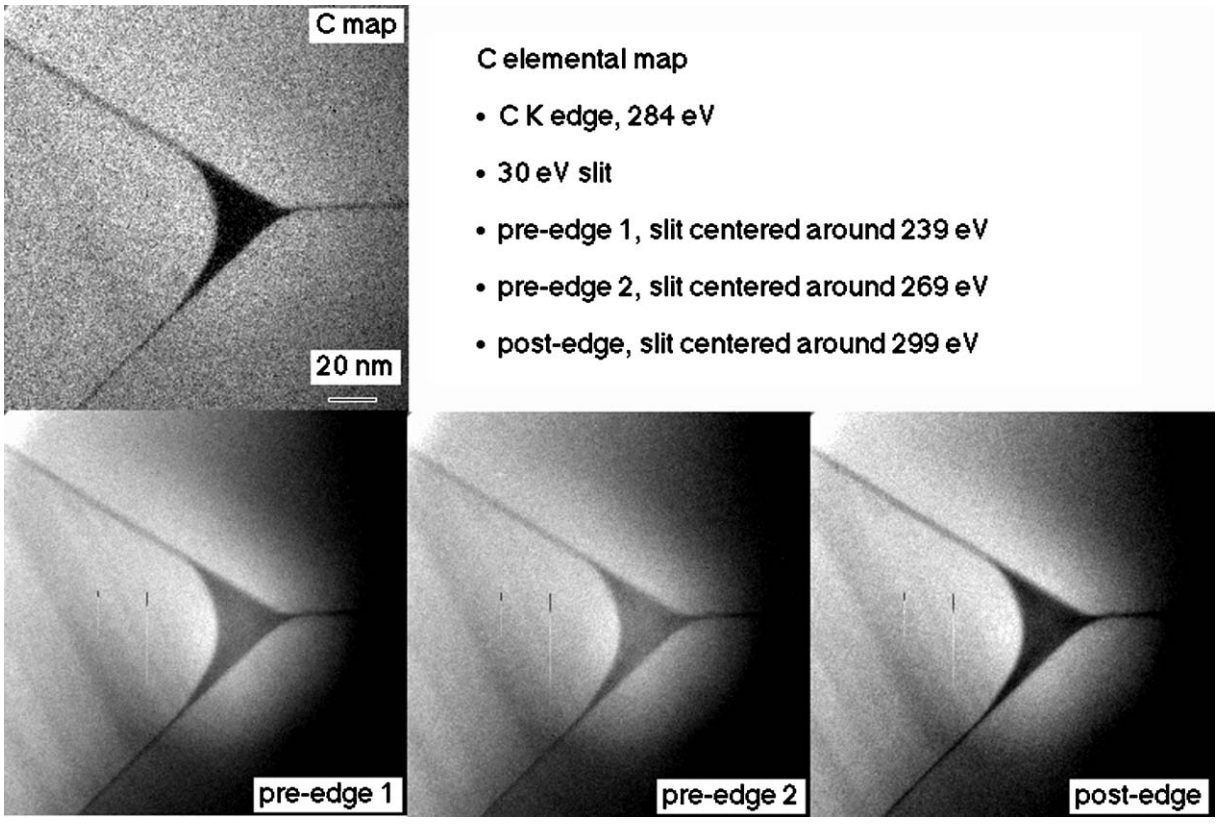

(a)

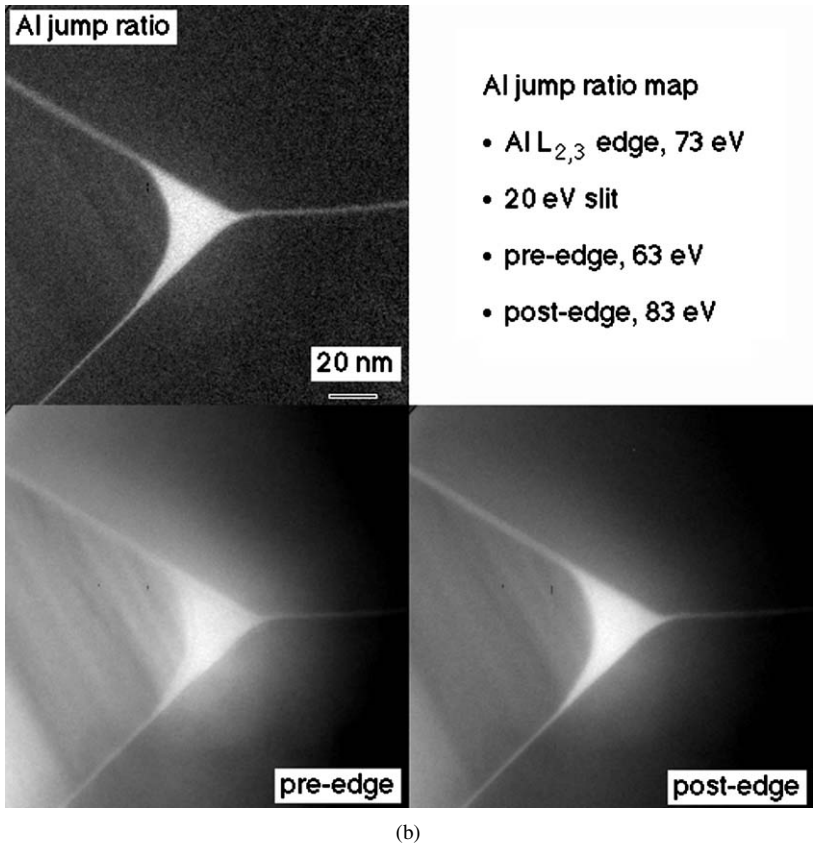

(b)

Figure 10 The computation of a carbon elemental map (a) and an aluminium jump ratio map (b) of a triple grain junction in a HIP:ed liquid phase sintered silicon carbide ceramic.

Jump ratio maps are computed by dividing a post-edge image by a pre-edge image. Artefacts that may be introduced by background modeling and subtraction are avoided by this method, and diffraction contrast cancels out to a large extent. Also, jump ratios result in elemental distribution images with a better signal to noise ratio. Electron spectroscopic images acquired for computing of an aluminium jump ratio map are shown in Fig. 10b.

5. The effect of metal oxide additives on Si_3N_4 grain morphology

5.1. Indirect observations

Work on Si_3N_4 ceramics densified by HIP with different combinations of smaller (up to around 5 wt%) additions of Al_2O_3, Y_2O_3 and ZrO_2 implied that the choice of metal oxide had an effect on grain size and shape, in addition to controlling the volume fraction of retained α-Si_3N_4 [14, 17]. It was established that an addition of Y_2O_3 promotes the α to β transformation, and also provides an isotropic liquid phase that allows the growth of faceted β-Si_3N_4 grains. It has, however, been indicated in the literature that yttrium results in a comparatively high viscosity of the liquid phase sintering medium [19]. Diffusion in an yttrium containing liquid would, hence, be relatively slow, and the solution/reprecipitation process would occur with a reduced material transport, and therefore a smaller contribution to the densification process. An addition of Al_2O_3, together with the Y_2O_3, will reduce the lowest eutectic temperature of the oxide system, from 1660 to 1345°C, and this would result in an increased volume fraction of liquid phase and thereby promote densification.

The microstructures of the Si_3N_4 ceramics fabricated with Al_2O_3 and/or undoped ZrO_2 appeared to have a different β-Si_3N_4 grain morphology. Predominantly rounded, and smaller, grain sections were observed in the TEM which suggested that the grains had a more equiaxed shape.

The relative α-Si_3N_4 contents and the apparent differences in β-Si_3N_4 grain shape had clear implications on the mechanical properties of these materials [17]. The development of a fibrous microstructure, as in the materials fabricated with additions of Y_2O_3, increased toughness, while the presence of retained α-Si_3N_4 resulted in a higher hardness.

5.2. Reconstruction of the three-dimensional microstructure

The effect of different metal oxide additives on β-Si_3N_4 grain growth and three-dimensional microstructure was later established for Si_3N_4 ceramics fabricated with a constant total molar fraction of oxide additives [24, 37]. The microstructures were characterized by quantitative microscopy and stereological methods as outlined in Section 4.1 above.

Results from SEM and TEM have demonstrated that the grain shape in many β-Si_3N_4 microstructures may, to a good approximation, be described by an hexagonal prism with a certain aspect ratio (length-to-width ratio) when the grains have been allowed to grow freely in an isotropic liquid phase environment [2, 30]. This is also illustrated by Fig. 1b, which shows prismatic β-Si_3N_4 grains protruding from a section subjected to excessive chemical etching. This shape reflects the hexagonal β-Si_3N_4 lattice, with the c-axis along the length of the prism, and the prism planes forming on the {10-10} crystal planes [51]. The hexagonal prism was, hence, used as a model for the β-Si_3N_4 grain shape in the assessment of the three-dimensional microstructure.

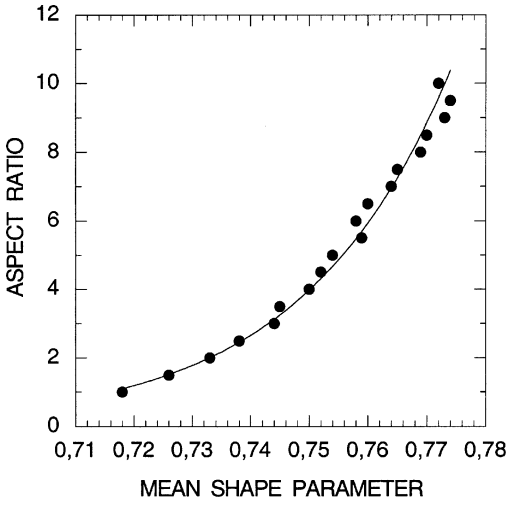

Figure 11 The mean shape parameter ($\bar{Q}$) obtained from computer simulations as a function of hexagonal prism aspect ratio. The prism facet width was set to 1 for all aspect ratios. From reference [52].

The average grain shape in the investigated microstructures was then determined by comparing results from quantitative microscopy of polished and etched sections with computer-generated two-dimensional stereological parameters of hexagonal prisms with different aspect ratios. The computer simulations showed that the mean value of the dimensionless shape parameter[1], $\bar{Q}$, which is independent of prism volume, is particularly sensitive to the aspect ratio of the hexagonal prism, see Fig. 11. $\bar{Q}$ is, thus, a suitable parameter for the determination of an average aspect ratio, i.e., an average β-Si_3N_4 grain shape [52]. Section parameter distributions for the average grain shape determined from $\bar{Q}$ were then obtained from computer simulations and used in a three-dimensional reconstruction of the microstructure as described in detail in reference [37].

The reconstructions showed that oxynitride glass network modifiers promote the development of high aspect ratio β-Si_3N_4 grains; an increased Y_2O_3/Al_2O_3 molar ratio results in an increased aspect ratio. The work also showed that the radius of the modifying cation affects the aspect ratio. The replacement of Y_2O_3 by Yb_2O_3 ($r(Yb^{3+}) = 0.868$ Å, and $r(Y^{3+}) = 0.900$ Å) results in a further increase of the aspect ratio, i.e., a reduced cation radius promotes an increase in aspect ratio. Oxynitride glass network modifiers also promote grain growth; increasing the Y_2O_3/Al_2O_3 molar ratio increases the mean grain size in the microstructure. It was also established that selecting a glass network modifying cation with a smaller radius results in an increased mean grain

[1] $Q = 4\pi A/U^2$, where A = individual intersect area of polygonal section, U = individual perimeter length of polygonal section.

volume and gives a microstructure with a more narrow grain size distribution [24].

6. The intergranular microstructure

The microstructure of a liquid phase sintered Si_3N_4- or SiC-based ceramic material contains, in general, an intergranular glassy phase present as thin grain boundary films merging into pockets at multi-grain junctions as shown in Figs 2 and 6a. This glass is a residue of the liquid phase sintering medium [10, 20, 53]. A reduced intergranular glass volume results when liquid phase constituents are incorporated into solid phases during sintering. This can be achieved through the formation of solid solutions, e.g., α- and β-sialon in Si_3N_4-based ceramics, or by the partitioning of secondary crystalline phases from the liquid phase sintering medium, see Fig. 12. Many of the secondary crystalline phases that form in liquid phase sintered silicon-based ceramics are, however, not stable at the high sintering temperature, and a post-densification heat treatment at a lower temperature may, therefore, be required in order to reduce the volume fraction of residual glass [1, 4, 7, 10, 20, 53–55].

The degree of secondary crystallization depends on factors such as the overall composition of the sintering additives and the temperature/time program during the densification or a post-densification heat treatment. Work has also shown that parameters such as the atmosphere during sintering and heat treatment, and an applied pressure during densification, may have an effect on the intergranular microstructure [20, 56, 57]. A complete crystallization is, however, generally not obtained, even if the chemistry of the starting powder mixture has been carefully designed, as shown in Fig. 3. The liquid and glass phases may support hydrostatical stresses, and these may present an obstacle to the crystallization of smaller liquid or glass volumes [58, 59].

A tailored starting powder composition containing metal oxide or nitride additives that can be incorporated into the solid phase, or form refractory crystalline grain boundary phases, is, hence, one way to a controlled intergranular microstructure. The intergranular microstructure in a liquid phase sintered silicon nitride based ceramic may be viewed as an oxynitride glass-ceramic. One way to controlling the intergranular microstructure would, hence, be to sinter with a combination of additives corresponding to an oxynitride glass that may be readily crystallized to a glass-ceramic after densification. It is, however, important that the overall composition results in secondary phases that are stable and oxidation resistant if the ceramic is going to be used at elevated temperatures. One other route to a minimized glass, and intergranular, volume is to reduce the amount of additives. This may, however, also require the application of an external pressure during sintering in order to achieve a fully dense body.

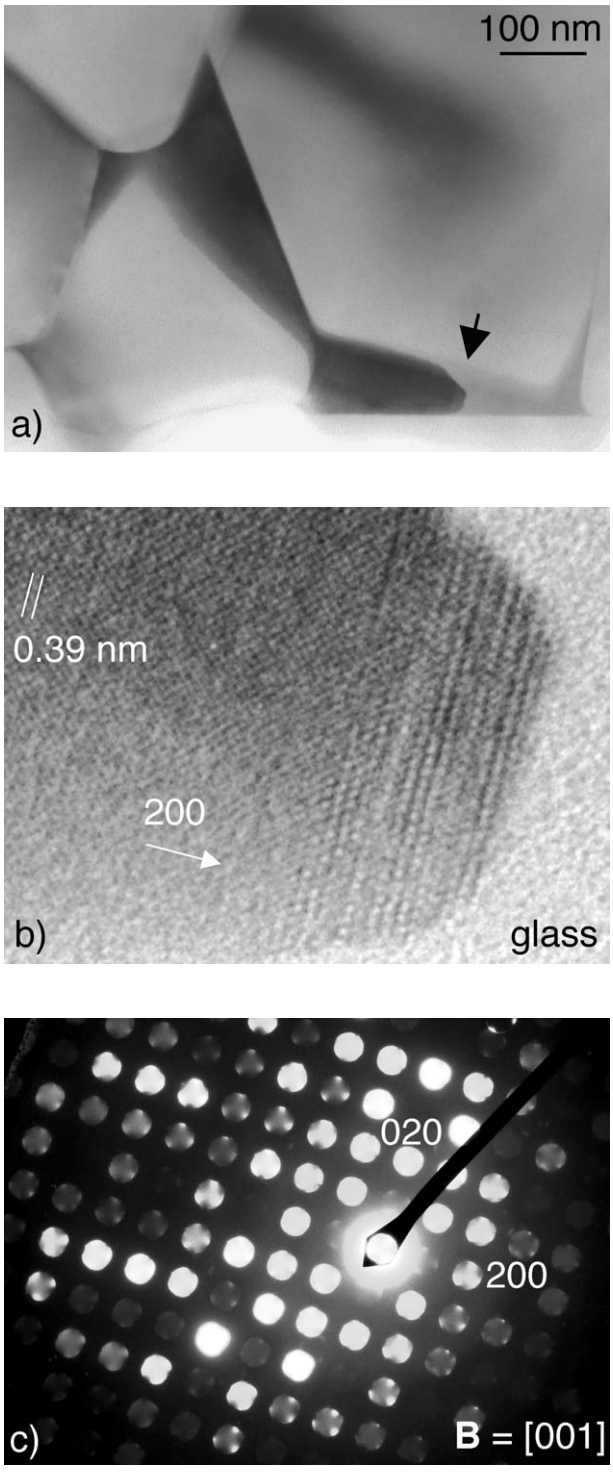

Figure 12 The crystallisation of tetragonal $Sm_2Si_{3-x}Al_xO_{3+x}N_{4-x}$ (mellilite) in a samarium α-sialon microstructure. The crystallisation front, arrowed in (a), had a faulted structure as shown in (b). This part became amorphous under the exposure to the electron beam in the TEM. The direction of the electron beam in the mellilite was close to [001] as shown by the micro-diffraction pattern in (c).

6.1. Pockets of residual glass in sialon microstructures

Fine probe EDX analysis in the FEGTEM has shown that the composition of residual glass pockets is generally not homogeneous [38, 51]. Grain growth during densification results in diffusion profiles and a shift in the average glass composition. This shift in composition results in a glass that is richer in additive cations, and this may promote the formation of secondary crystalline phases during a prolonged holding time at the densification temperature [24, 51]. Elemental concentration profiles across β'- or α'-Si_3N_4 facets into pockets of residual glass have shown that the cations

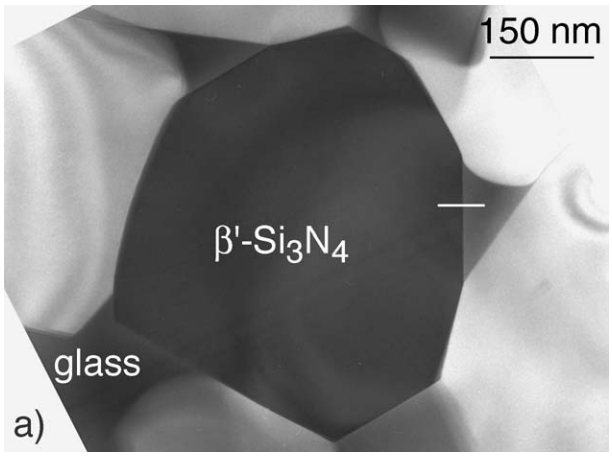

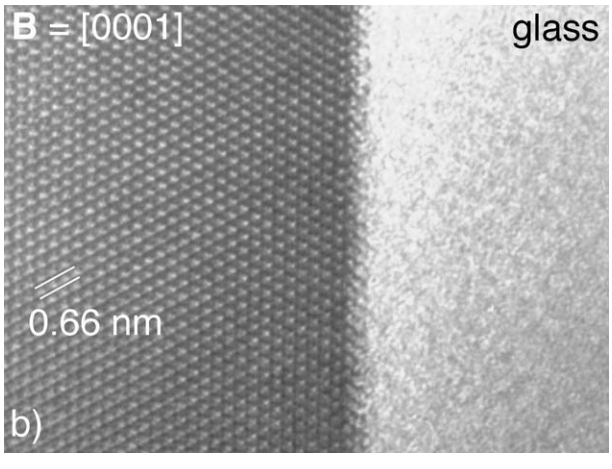

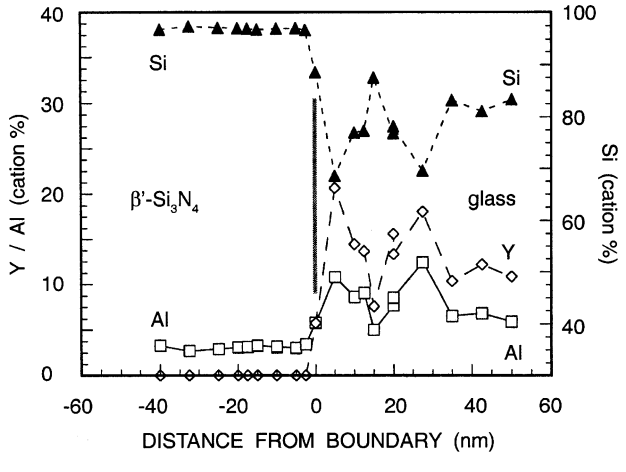

Figure 13 β'-Si_3N_4 grain (a) oriented with the *c*-axis of the hexagonal lattice parallel to the incident electron bem. Cation concentration profiles across the {10-10} facet, indicated in (a) and detailed in (b), are shown in (c). The profiles were obtained from EDX point analyses in a FEGTEM using an electron probe with a nominal FWHM of around 0.7 nm.

from the sintering additives are anti-correlated with the silicon in the residual oxynitride glass. This has been observed for both glass network formers (Al^{3+}) and network modifiers (Y^{3+}, Sm^{3+}), see Figs 13 and 14. As expected, these profiles show that there is an anti-correlation of aluminum with silicon also in the sialon grains.

The silicon nitride microstructure shown in Fig. 13 developed during gas pressure sintering of a powder compact containing a total of 9.5 mol% Y_2O_3 and

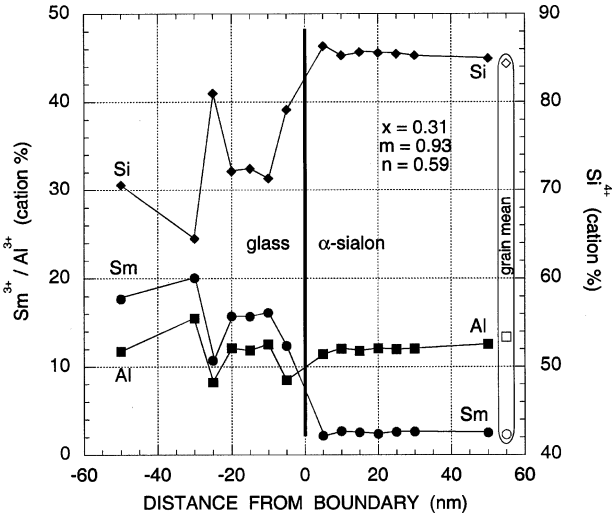

Figure 14 Cation concentration profiles across a samarium α-sialon {10-10} prism plane growing into a pocket of residual glass. The EDX point analyses were carried out in a FEGTEM using an electron probe with a nominal FWHM of around 0.7 nm.

Al_2O_3 with a Y_2O_3/Al_2O_3 molar ratio corresponding to that of the Y, Al-garnet (YAG), $5Al_2O_3 \cdot 3Y_2O_3$ [24, 51]. A certain amount of aluminum was incorporated into the β-Si_3N_4 lattice, resulting in the formation of a dilute β'-Si_3N_4, but a major part of the

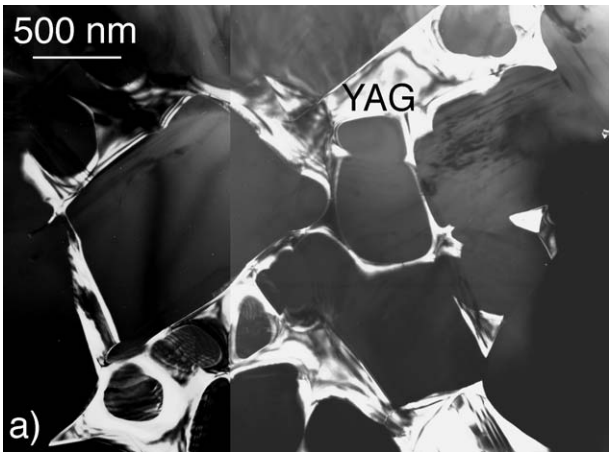

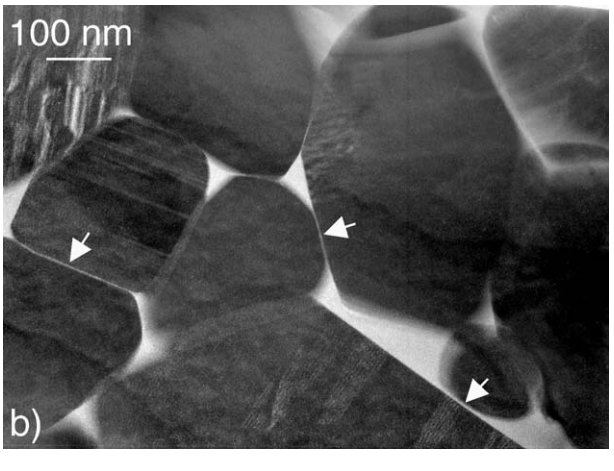

Figure 15 The microstructure of silicon carbide ceramics liquid phase sintered with the addition of 1.3 wt% Al_2O_3 and 1.7 wt% Y_2O_3 after (a) pressureless sintering and (b) HIP. The microstructure in (a) contains intergranular Y, Al-garnet (YAG), while the intergranular microstructure in (b) is amorphous (TEM centered dark field images). Thin grain boundary films of residual glass are arrowed in (b).

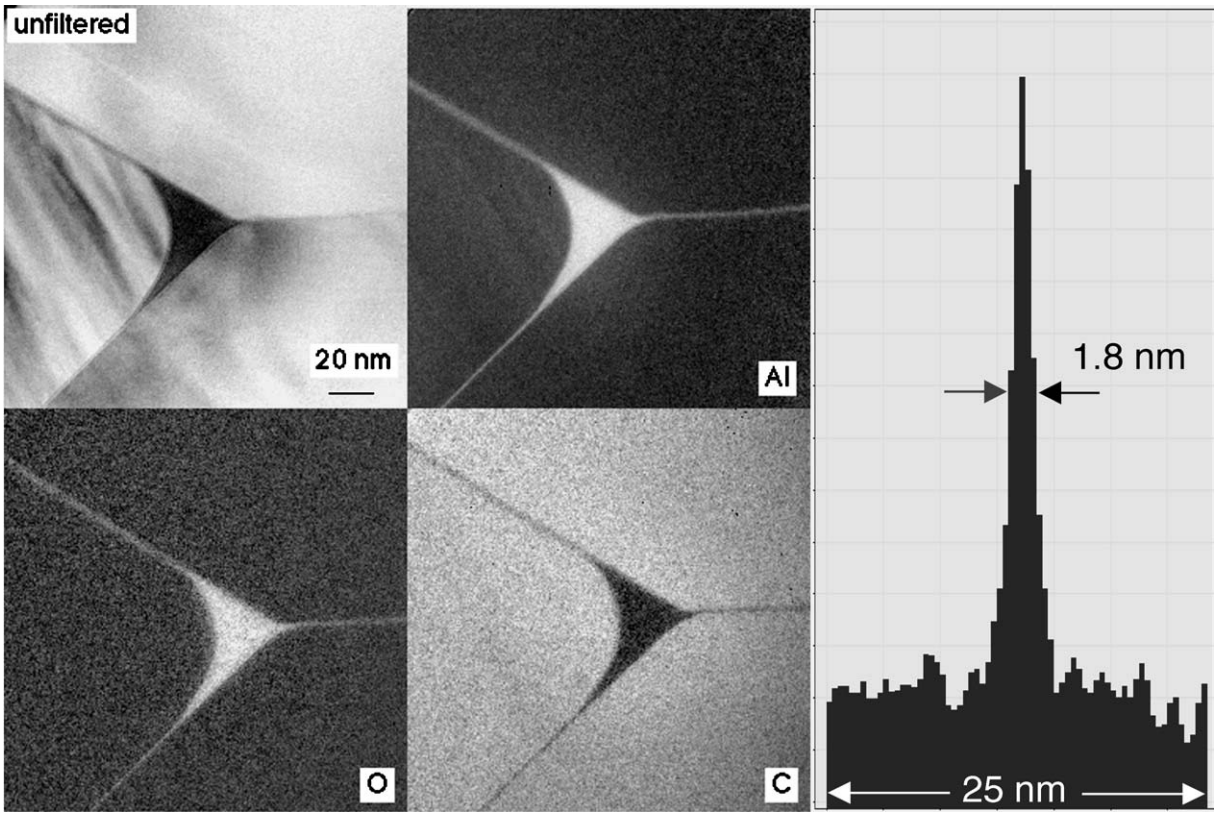

Figure 16 Elemental distribution images of a triple grain junction in a silicon carbide ceramic HIP:ed with the addition of 1.3 wt% Al_2O_3 and 1.7 wt% Y_2O_3. The computation of the carbon and aluminum images is shown in Fig. 10. The intensity distribution in the aluminum image across the edge-on grain boundary film indicated a film thickness of 1.8 nm.

aluminum, as well as the yttrium, had to diffuse away from the moving interface, into the remaining liquid volume, in order for grain growth to take place. The self-diffusivity of the oxynitride liquid phase constituents at the sintering temperature would, hence, affect the grain growth rate. These observations are consistent with the grain growth exponent of 3 (diffusion controlled grain growth) that was determined from three dimensional reconstructions of the β-sialon microstructure after different holding times at the sintering temperature [24].

One other example indicating that sialon grain growth is rate controlled by diffusion through the liquid phase sintering medium is shown in Fig. 14. The growing α'-Si_3N_4 grain incorporates some samarium, and has an average aluminum cation fraction that is only marginally higher than that of the residual glass pocket. This results in a significantly increased concentration of samarium, accompanied by a slight reduction in the aluminum concentration, in the glass just outside the moving interface. It may also be noted that the interstitial cation in the α'-Si_3N_4 structure (Sm^{3+}) seems to be anti-correlated with silicon.

6.2. Crystallisation of secondary phases in α-SiC microstructures

Pressureless sintering and HIP of α-SiC green bodies containing additions of Y_2O_3 and Al_2O_3, with an Y_2O_3/Al_2O_3 ratio corresponding to that of the Y, Al-garnet ($5Al_2O_3{\cdot}3Y_2O_3$), demonstrated that the sintering atmosphere as well as an applied pressure have an effect on the development of the intergranular microstructure [20]. Pressureless sintering was carried out in a SiC/Al_2O_3 protective powder bed in an argon atmosphere at 1880°C for 2 or 4 h. This resulted in the partitioning of Y, Al-garnet and α-Al_2O_3 from the liquid phase sintering medium, and only smaller volumes of residual glass were present in the microstructure. The glass was concentrated to thin intergranular films and to a limited number of smaller (<20 nm) pockets.

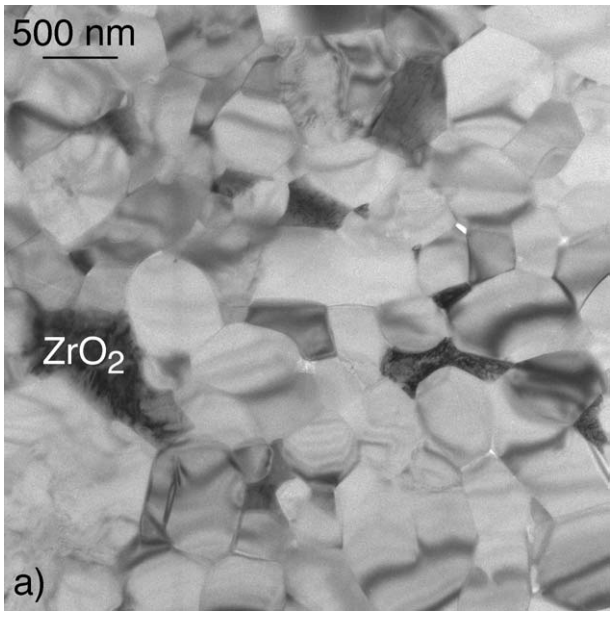

Figure 17 The microstructure of a Si_3N_4 ceramic HIP:ed 1750°C with the addition of 5 wt% ZrO_2(+3 mol% Y_2O_3) and 2 wt% Al_2O_3. The microstructure contains an extremely small volume fraction of residual glass.

These pockets were rich in silicon, aluminum and oxygen, and contained also smaller amounts yttrium and impurities, e.g., calcium. The yttrium content of these pockets was, however far too low for the crystallization of the Y, Al-garnet.

Partitioning of the Y, Al-garnet, Fig. 15a, resulted in neighbouring pockets with the same crystallographic orientation. This suggests that the crystallisation involved comparatively few nucleation sites, and that the garnet grew in a three-dimensional intergranular network. It was proposed that the formation of α-Al_2O_3 was promoted by a transport of gaseous AlO and Al_2O from the powder bed into the SiC material. The formation of AlO and Al_2O would be associated with a decomposition of the Al_2O_3 in the powder bed by carbon, which is generally present in the surrounding environment during pressureless sintering. The incorporation of Al_2O_3 from the powder bed into the intergranular microstructure was also observed for SiC(+Y_2O_3) ceramics pressureless sintered under the same conditions, but without the addition of Al_2O_3.

HIP of the SiC(+5Al_2O_3·3Y_2O_3) composition at 1800°C under a pressure of 160 MPa resulted in a completely different microstructure, see Figs 15b and 16. The crystallisation of the liquid phase sintering medium was suppressed; Y, Al-garnet did not partition although the Y/Al ratio of analyzed residual glass pockets varied around that of the garnet.

7. Si_3N_4/ZrO_2 composite ceramics

A secondary crystalline phase may act as a reinforcement. An addition of ZrO_2 to Si_3N_4 is not only an effective sintering additive, but may also result in a composite Si_3N_4 ceramic microstructure, see Figs 5, 17 and 18, where grains of ZrO_2 act as a toughening and strengthening agent [13, 14, 57, 60]. In addition, as shown in Figs 5c and 17, the partitioning of a ZrO_2 structure from the liquid phase sintering medium makes it possible to form Si_3N_4-based ceramics with extremely small volume fractions of residual glass present only as thin grain boundary films between grains of Si_3N_4 and/or ZrO_2 [29, 57]. A zirconium containing oxynitride liquid phase sintering medium may also promote the development of high aspect ratio β-Si_3N_4 grains, which contributes further to the toughness of the ceramic.

The α to β-Si_3N_4 transformation in zirconium rich liquid phase sintering media is often associated with the formation of Si_2N_2O [13, 14, 29, 60]. This was also the case for the pressureless sintered Si_3N_4/ZrO_2 material in Fig. 5. The crystallisation of Si_2N_2O during the α to β transformation was evident from X-ray diffraction data of partially sintered compacts, and the presence of well-defined larger, elongated, Si_2N_2O grain sections in SEM and TEM images. The partitioning of Si_2N_2O, in addition to β-Si_3N_4, would increase the relative nitrogen content of the remaining liquid, and this may

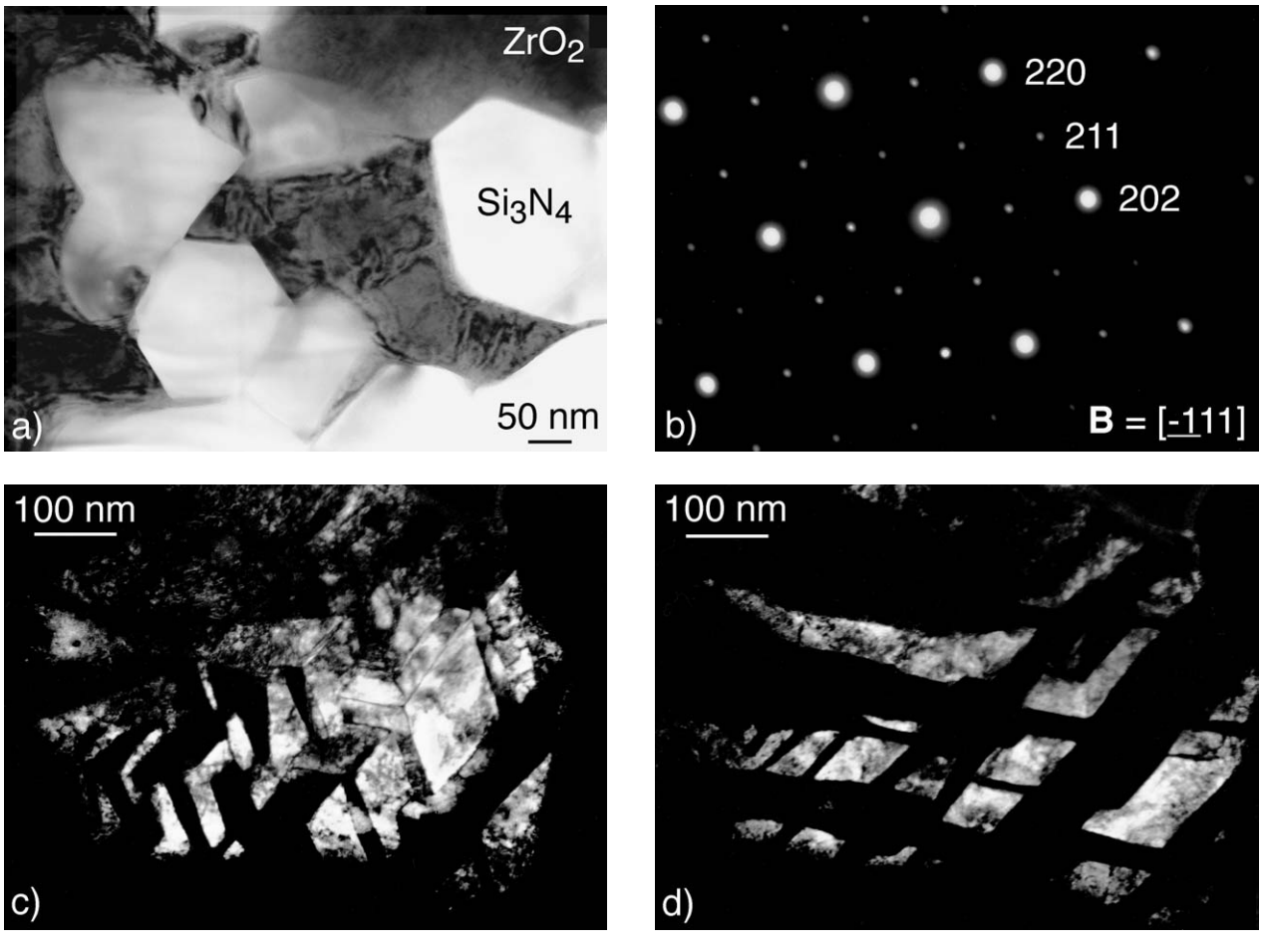

Figure 18 The microstructure of a composite Si_3N_4 + 30 wt% ZrO_2(+3 mol% Y_2O_3) ceramic pressureless sintered at 1650°C. Faceted Si_3N_4 grain sections are separated by irregularly shaped grains of Y_2O_3 containing ZrO_2 (a). The ZrO_2 grains consist of domains with the tragonal t' structure as shown by the selected area electron diffraction pattern in (b). Centered dark field imaging using different {112} reflections revealed the domain structure of t′, (c) and (d).

have an effect on the structure and properties of the ZrO_2 phase.

The ZrO_2 may incorporate nitrogen into its structure during partitioning from the liquid phase sintering medium whereby an oxidation-prone zirconium-oxynitride solid solution is formed [60]. Work has shown that the simultaneous addition of Y_2O_3, or the use of an Y_2O_3 partially stabilized ZrO_2 starting powder, will reduce the nitrogen uptake of the $ZrO_2(+Y_2O_3)$ structure that partitions during sintering [57, 60, 61]. It was also established that the sintering atmosphere has an effect on the anion lattice [57]. HIP resulted in ZrO_2 structures with a better high temperature stability than after pressureless sintering, which infers that the nitrogen atmosphere around the Si_3N_4 powder compact during pressureless sintering results in an increased nitrogen content of the liquid and thereby of the ZrO_2 grains that form in the material. Si_3N_4/ZrO_2 ceramics have also been fabricated with a smaller addition of Al_2O_3 as sintering additive. This promotes the formation of a dilute β'-Si_3N_4 structure which will adjust the oxygen/nitrogen ratio of the liquid phase sintering medium.

The composition and structure of the ZrO_2 will determine the toughening mechanisms that may be activated [62]. Transformation toughening may take place if a transformable metastable tetragonal structure is retained in the sintered material. This structure will transform to the monoclinic structure when the mechanical constraints imposed on the ZrO_2 grains are released in a stress field. The non-transformable t′ structure, which consists of tetragonal domains separated by anti-phase domain boundaries, see Fig. 18, may contribute to toughness by ferroelastic domain switching. The retention of these tetragonal structures to room temperature is realized through the incorporation of a cation with a lower valence state, e.g. Y^{3+}, into the ZrO_2 structure.

8. Glassy grain boundary films

Even if a substantial crystallisation of the intergranular regions in a liquid phase sintered silicon-based ceramic microstructure has been achieved, thin intergranular films of residual glass generally remain. Electron energy filtering and fine probe EDX analysis has demonstrated that the glassy grain boundary films in SiC and Si_3N_4 based microstructures are rich in elements originating from the metal oxide/nitride sintering additives, but depleted in carbon and nitrogen, respectively [24].

As discussed above, pressureless sintering of SiC with additions of Y_2O_3 and Al_2O_3 makes it possible to

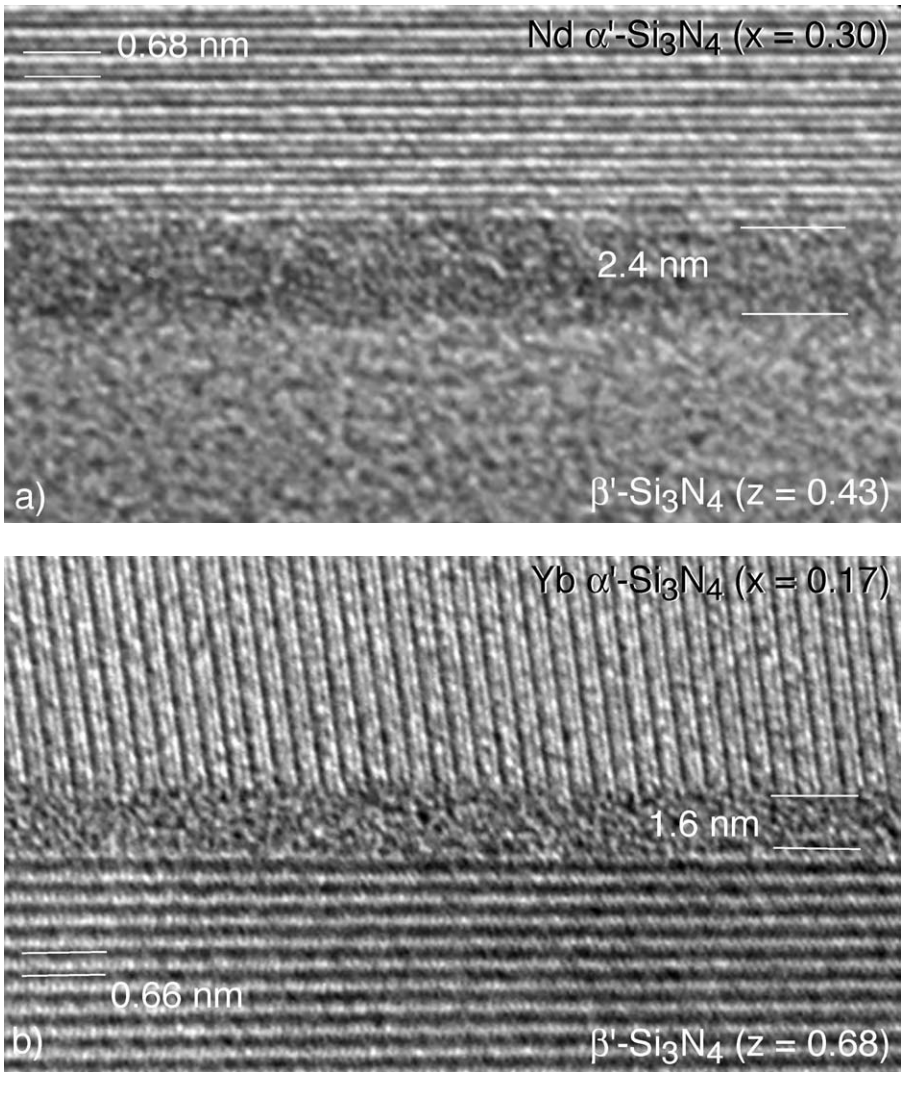

Figure 19 Intergranular films of residual glass in duplex α/β sialons fabricated with the addition of (a) Nd_2O_3 and (b) Yb_2O_3.

obtain a substantial crystallisation of the liquid phase sintering medium. Thin films of residual glass were, however, separating the secondary Y, Al-garnet and α-Al_2O_3 structures from adjacent grains of SiC [20, 24]. Thin films of residual glass, with a varying cation content, were present also at SiC/SiC grain boundaries [20, 24]. Combined high resolution analytical and spatial information obtained from electron energy filtered images recorded around the carbon K, oxygen K and aluminum $L_{2,3}$ edges in the EEL spectrum showed that glassy grain boundary films, as well as the occasional smaller pockets of residual glass, were rich in oxygen and aluminum, but depleted in carbon, as in the HIP:ed SiC microstructure shown in Fig. 16. Intensity profiles integrated along elemental images of edge-on grain boundaries, as in the aluminum jump ratio map in Fig. 16, indicated average film thicknesses in the range 1.5 to 1.8 nm. This is consistent with results from defocus Fresnel imaging [20]. EDX showed that thin films merging into smaller yttrium and impurity cation containing glass pockets contained also these elements.

High resolution TEM of Si_3N_4-based microstructures has demonstrated that the film thickness depends upon the overall chemistry of the ceramic microstructure as well as the structure and composition of neighbouring grains. The intergranular films in β'-Si_3N_4/ZrO_2 composite ceramic microstructures may be as thin as 0.9 to 1.0 nm when the residual glass is present only at the grain boundaries [57]. Some sialon microstructures show significantly larger film thicknesses of around 2.4 nm, even when a substantial part of the liquid phase constituents have been incorporated into the β'- and/or α'-Si_3N_4 solid solutions, or other sialon structures, so that the volume fraction of residual glass is extremely small [39, 63].

A smaller network modifying cation tend to reduce the average thickness of the intergranular glass film [63, 64]. The replacement of Nd_2O_3 by Yb_2O_3 in the fabrication of duplex α/β-sialon ceramics resulted in a reduced film thickness, see Fig. 19. The intergranular films in the microstructure containing the larger Nd^{3+} ($r(Nd^{3+}) = 0.983$ Å) were typically around 2.4 nm, while the smaller Yb^{3+} ($r(Yb^{3+}) = 0.868$ Å) resulted in residual glass films in the range 1.6 to 1.9 nm thick. The small variation in measured film thickness within a microstructure was accompanied by a variation in the local α- and β-sialon substitution levels.

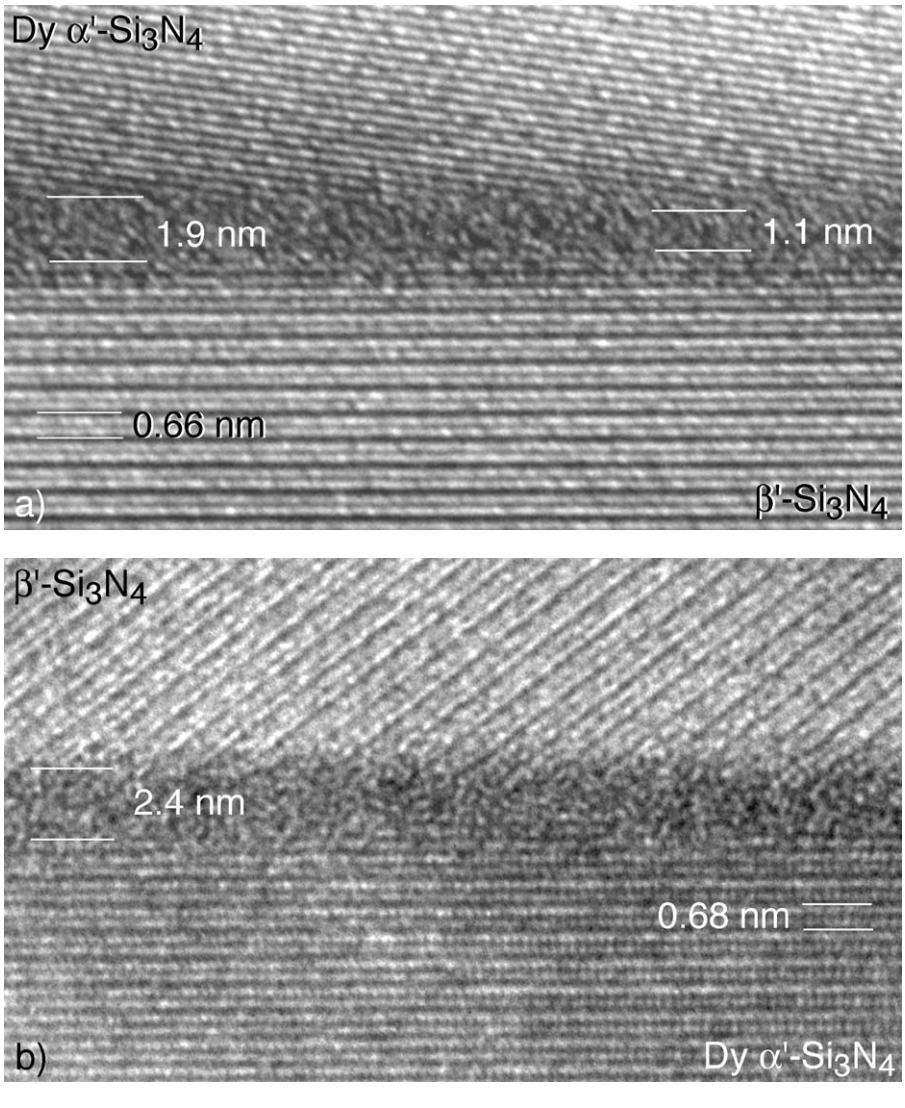

Figure 20 Intergranular films of residual glass in a duplex α/β sialon fabricated with the addition of Dy_2O_3. The grain boundary in (a) has a film thickness that varies significantly along the boundary, while the thickness of the grain boundary film in (b) shows only smaller variations around an average thickness of 2.4 nm.

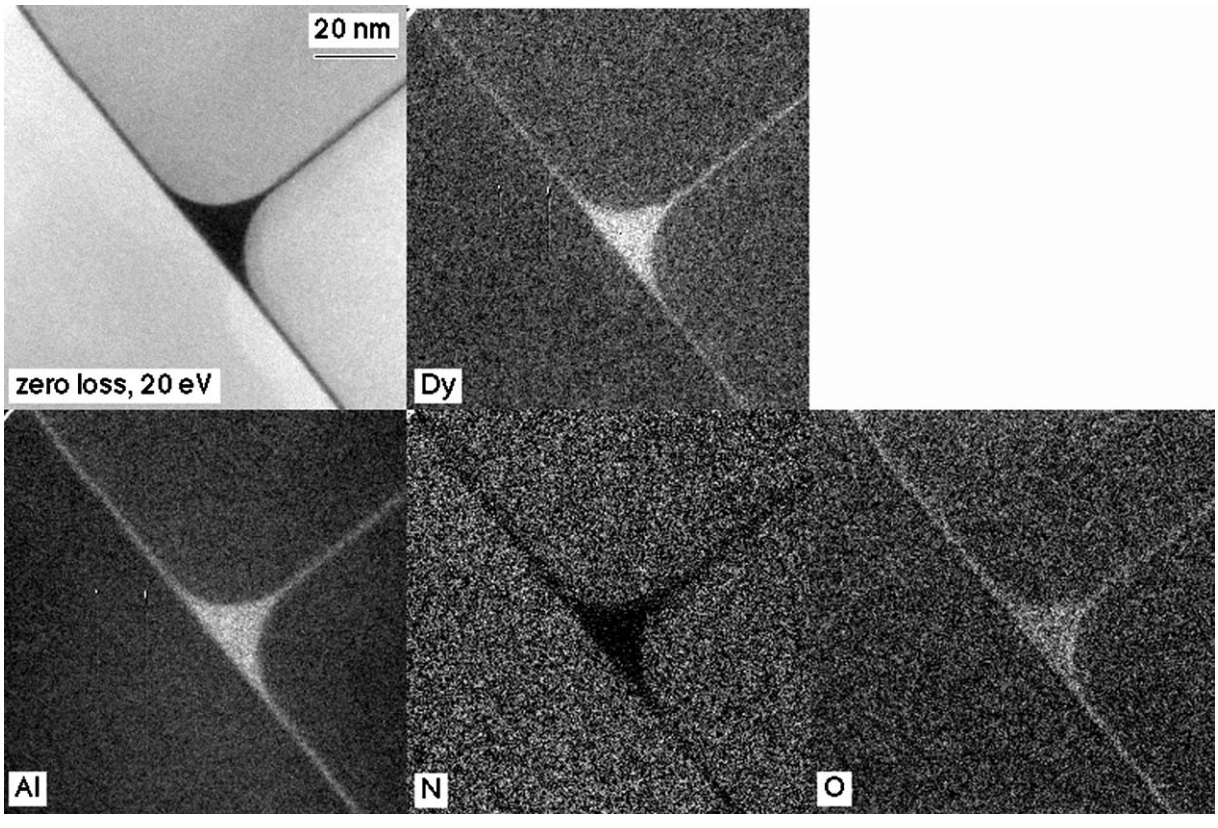

Figure 21 Elemental distribution images of a triple grain junction in a dysprosium α-sialon microstructure.

The thickness of the residual glass films may, however, vary significantly within a microstructure, both between boundaries and within a particular boundary. These observations are in contrast to models suggesting that there is a constant grain boundary film thickness throughout a microstructure [65–67]. The radius of Dy^{3+} is 0.912 Å which suggests that the use of Dy_2O_3 instead of Yb_2O_3 or Nd_2O_3 in the fabrication of the duplex sialons discussed above would result in a film thickness in between what was observed for the smaller Yb^{3+} and larger Nd^{3+} cations. This material showed, however, a wide spread in film thickness. Fig. 20a shows an example of an α/β grain boundary where the film thickness varies between 1.1 and 1.9 nm over a distance of 20 nm along this section of the boundary. A significantly thicker film, 2.4 nm, separating an α'- and a β'-Si_3N_4 grain in the same material is shown in Fig. 20b. This microstructure showed a pronounced variation in the local substitution levels of the α'- and β-Si_3N_4 grains, which can be expected to contribute to the observed spread in grain boundary film thickness.

Electron spectroscopic imaging and subsequent computation of elemental distribution images has been performed for a number of α- and duplex α/β-sialons fabricated with additions of Sm_2O_3, Dy_2O_3 or Yb_2O_3. The electron spectroscopic images were recorded around the nitrogen K, oxygen K, aluminum $L_{2,3}$ and rare earth element $N_{4,5}$ edges in the EEL spectrum [24]. The elemental distribution images clearly demonstrated the concentration of the α' stabilizing cation, aluminum and oxygen to the glassy grain boundary films, and that these films also have a reduced nitrogen content. These results are in accordance with elemental concentration profiles across α'/α', α'/β' and β'/β' grain boundaries, which showed an enrichment of aluminum and the rare earth element to the glassy grain boundary film [24]. These profiles also revealed a significant variation in the α' and β' substitution levels on a nanometer scale, which reflects the extensive solid solution of the sialon phases. An example of elemental distribution images of a dysprosium α-sialon microstructure is shown in Fig. 21, and elemental profiles across a grain boundary the same microstructure are shown in Fig. 22.

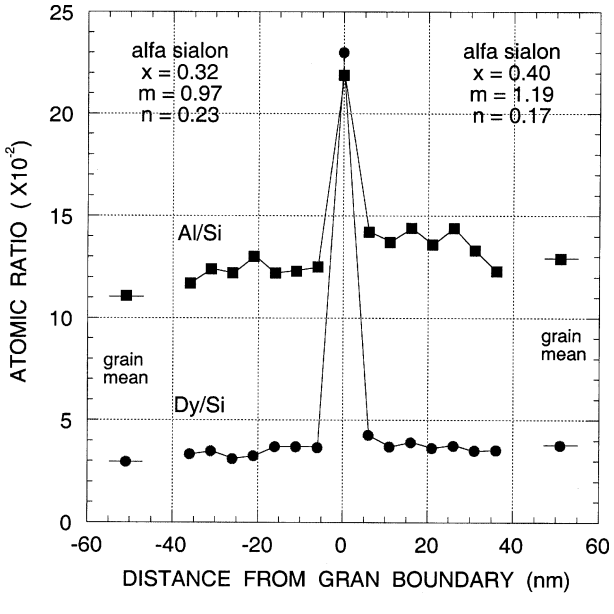

Figure 22 Atomic ratio profiles, obtained from step by step EDX point analyses, across a grain boundary film in a dysprosium α-sialon microstructure. An electron probe with a nominal FWHM of 0.7 nm was used for the acquisition of the EDX spectra in a FEGTEM.

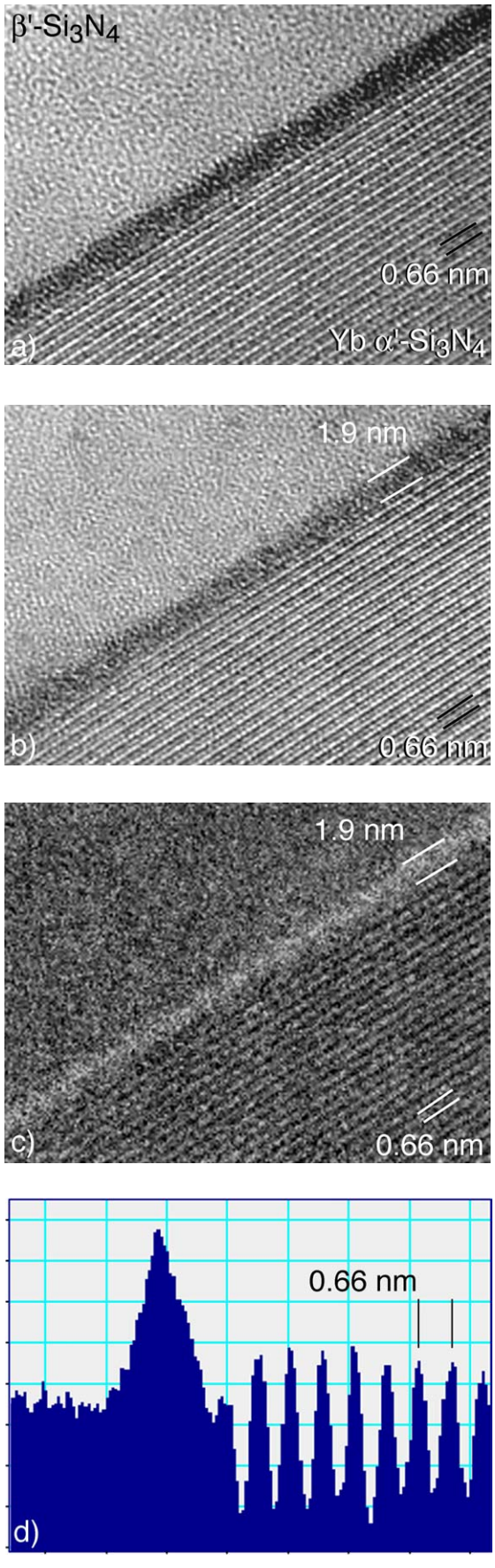

Figure 23 Unfiltered (a) and zero loss (b) images of an edge-on α'-/β'-Si_3N_4 grain boundary in a duplex ytterbium sialon microstructure. The zero loss image was acquired with an energy selecting slit of 20 eV. The jump ratio map across the ytterbium N edge (c) shows the concentration of ytterbium to the glassy grain boundary film and the preservation of phase contrast in the α' grain. The film thickness was estimated to 1.9 nm from an intensity profile (d) integrated along 30 nm of the grain boundary in the jump ratio map.

Phase contrast may be preserved in low electron energy loss images because of Bragg scattering of inelastically scattered electrons [46, 50]. Under such conditions, computed elemental distribution images will also show phase contrast as illustrated by the jump ratio map across the ytterbium N edge in Fig. 23. The map shows the segregation of ytterbium to an α'-/β'-Si_3N_4 grain boundary in a duplex sialon microstructure, and also the retention of phase contrast in the α-sialon grain. This grain is in a strongly diffracting orientation as shown by the unfiltered and zero loss images, and {10-10} lattice fringes are running parallel to the grain boundary. The unfiltered and zero loss images also show that the transition between the α' grain and the glass film is not well defined. The absorption contrast in these images, due to the segregation of ytterbium to the glassy grain boundary film, made it possible to estimate the average film thickness to 1.9 nm using the α'{10-10}

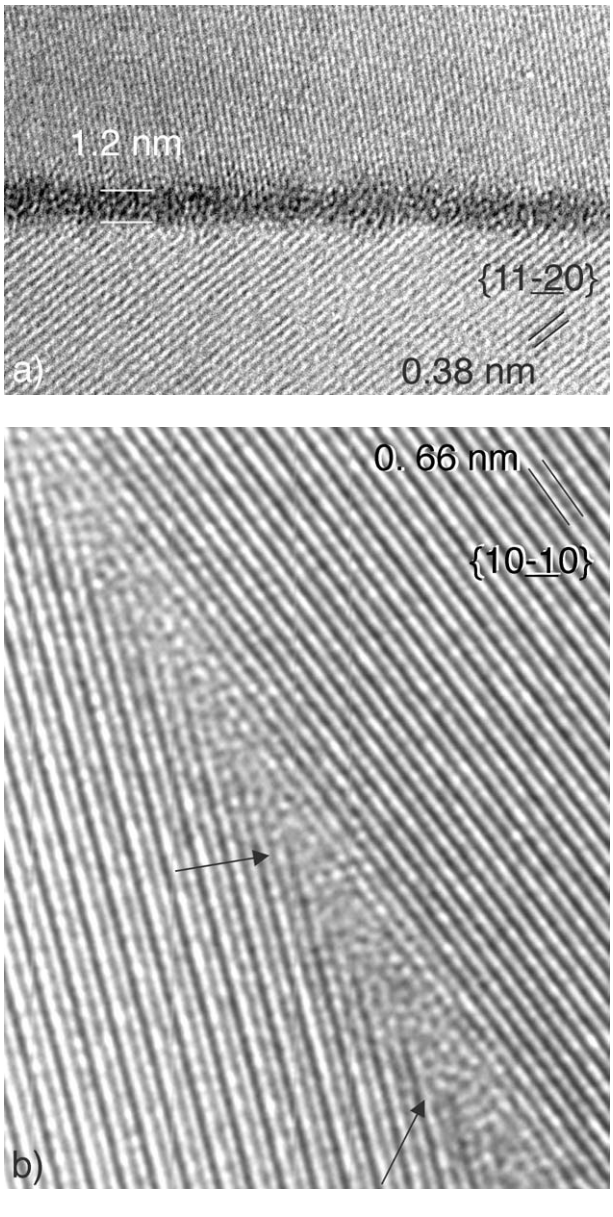

Figure 24 Grain boundary films in a silicon nitride ceramic gas pressure sintered with the addition of 3 wt% Y_2O_3. The boundary in (a) has an average film thickness of 1.2 nm. Within the resolution of the image (3.3 nm), the grains in (b) seem to be in direct contact; only some local disorder is observed between the arrows.

lattice fringes (interplanar spacing of 0.66 nm [33]) for internal calibration. An estimate of grain boundary film thickness was also made from a 10 nm intensity profile integrated along 30 nm of the grain boundary in the ytterbium jump ratio map using the α'{10-10} lattice fringes in the map for calibration. This gave a value of 1.9 nm, consistent with the measurements in the unfiltered and zero loss images.

Different grain boundary morphologies have also been observed within a microstructure where solid solutions can not form. Si_3N_4 gas pressure sintered with 3 wt% Y_2O_3 had typically a grain boundary film thickness of 1.1–1.2 nm, see Fig. 24a. These films were rich in yttrium and oxygen, and contained frequently also some impurities, e.g., calcium. A rather different type of boundary was, however, also observed in this microstructure. Fig. 24b shows a high resolution image of a boundary oriented edge on in the TEM. Contrast from a set of {20-20} fringes corresponding to a lattice spacing of 0.33 nm are clearly visible in both grains. Within the resolution of the image, the grains seem to be in direct contact along a substantial part of the boundary; only some local disorder is observed.

9. Concluding remarks

Quantitative microscopy together with analytical and high resolution transmission electron microscopy provides important information for a deeper understanding of the development of microstructure in liquid phase sintered silicon based ceramics. The combined information from different imaging, diffraction and spectroscopic methods in the TEM is required for a qualitative and quantitative chemical and structural characterization of small volumes in the microstructure. Analytical and spatial information from regions of the size 1 to 2 nm can be obtained by electron spectroscopic imaging and subsequent computation of elemental distribution images.

Acknowledgements

Collaboration with colleagues and former students at the Swedish Ceramic Institute, the Ceramics Research Unit, University of Limerick, Ireland, the Arrhenius Laboratory, University of Stockholm and the Departments of Experimental Physics and Engineering Metals at Chalmers University of Technology is highly appreciated.

References

1. F. F. LANGE, *Int. Met. Rev.* **1** (1980) 1.
2. *Idem.*, *J. Amer. Ceram. Soc. Bull.* **62** (1983) 1369.
3. G. ZIEGLER, J. HEINRICH and G. WÖTTING, *J. Mater. Sci.* **22** (1987) 3041.
4. K. H. JACK, "Ceramics and Civilization, Vol. III: High-Technology Ceramics" (American Ceramic Society, Columbus, OH, 1986) p. 259.
5. Z. C. JOU, V. VIRKAR and R. A. CUTLER, *J. Mater. Res.* **6** (1991) 1945.
6. R. RAJ, *J. Amer. Ceram. Soc.* **76** (1993) 2147.
7. R. A. CUTLER and T. B. JACKSON, in Proceedings of the 3rd International Symposium on Ceramic Materials and Components for Engines, edited by V. J. Tennery (American Ceramic Society, Westerville, OH, 1989) p. 309.
8. R. A. ALLIEGRO, L. B. COFFIN and J. R. TINKLEPAUGH, *J. Amer. Ceram. Soc.* **39** (1956) 386.
9. H. TANAKA, in "Silicon Carbide Ceramics", edited by S. Somiya and Y. Inomata (Elsevier Applied Science, London, 1991) p. 213.
10. M. H. LEWIS and R. J. LUMBY, *Powder Metall.* **26** (1983) 73.
11. L. CORDREY, D. E. NIESZ and J. SHANEFIELD, in "Sintering of Advanced Ceramics", edited by C. A. Handwerker, J. E. Blendell and W. Kaysser (American Ceramic Society, Inc., Westerville, Ohio, 1990) p. 618.
12. M. H. LEWIS, G. LENG-WARD and C. JASPER, *Ceram. Powder Sci.* **2** (1988) 1019.
13. L. K. L. FALK and K. RUNDGREN, *J. Amer. Ceram. Soc.* **75** (1992) 285.
14. M. KNUTSON-WEDEL, L. K. L. FALK and T. EKSTRÖM, *J. Hard Mater.* **3** (1992) 435.
15. P. F. BECHER, *J. Amer. Ceram. Soc.* **74** (1991) 255.
16. B. S. B. KARUNARATNE and M. H. LEWIS, *J. Mater. Sci.* **15** (1980) 449.
17. E. M. KNUTSON-WEDEL, L. K. L. FALK, H. BJÖRKLUND and T. EKSTRÖM, *ibid.* **26** (1991) 5575.
18. I. P. TUERSLEY, G. LENG-WARD and M. H. LEWIS, in "Engineering with Ceramics", edited by R. Morrell (British Ceramic Society, 1990) p. 231.
19. S. HAMPSHIRE and K. H. JACK, in "Special Ceramics 7", edited by D. Taylor and P. Popper (British Ceramic Research Association, Stoke-on-Trent, 1981) p. 37.
20. L. K. L. FALK, *J. Eur. Ceram. Soc.* **17** (1997) 983.
21. S. HAMPSHIRE, R. A. L. DREW and K. H. JACK, *Phys. Chem. Glass.* **26** (1985) 182.
22. W. D. KINGERY, *J. Appl. Phys.* **30** (1959) 301.
23. E. Y. SUN, P. F. BECHER, C.-H. HSUEH, S. B. WATERS, K. P. PLUCKNETT, K. HIRAO and M. BRITO, *J. Amer. Ceram.* Soc. **81** (1998) 2831.
24. H. BJÖRKLUND, L. K. L. FALK, K. RUNDGREN and J. WASÉN, *J. Eur. Ceram. Soc.* **17** (1997) 1285.
25. H. BJÖRKLUND and L. K. L. FALK, *ibid.* **17** (1997) 13.
26. P. VILLARS and L. D. CALVERT, in "Pearson's Handbook of Crystallographic Data for Intermetallic Phases" (ASM, Metals Park, OH, 1985) Vol. 1, p. 610.
27. D. HARDIE and K. H. JACK, *Nature* **180** (1957) 332.
28. S. HAMPSHIRE, H. K. PARK, D. P. THOMPSON and K. H. JACK, *ibid.* **274** (1978) 880.
29. L. K. L. FALK, *Mater. Forum* **17** (1993) 83.
30. M. H. LEWIS, B. D. POWELL, P. DREW, R. J. LUMBY, B. NORTH and A. J. TAYLOR, *J. Mater. Sci.* **12** (1977) 61.
31. K. H. JACK, in "Progress in Nitrogen Ceramics", edited by F. L. Riley (Martinus Nijhoff Publishers, The Hague, 1983) p. 45.
32. T. EKSTRÖM, L. K. L. FALK and Z.-J. SHEN, *J. Amer. Ceram. Soc.* **80** (1997) 301.
33. L. K. L. FALK, Z.-J. SHEN and T. EKSTRÖM, *J. Eur. Ceram. Soc.* **17** (1997) 1099.
34. D. M. SCHWARTZ, *J. Microscopy* **96** (1972) 25.
35. J. WASÉN and R. WARREN, *Metallography* **20** (1987) 431.
36. *Idem.*, *Mater. Sci. Tech.* **5** (1989) 222.
37. R. WARREN and N. V. NAUMOVICH, *J. Microscopy* **110** (1977) 113.
38. H. BJÖRKLUND, J. WASÉN and L. K. L. FALK, *J. Amer. Ceram. Soc.* **80** (1997) 3061.
39. L. K. L. FALK, *J. Eur. Ceram. Soc.* **18** (1998) 2263.
40. D. R. CLARKE, *Ultramicroscopy* **4** (1997) 33.
41. M. K. CINIBULK, H.-J. KLEEBE and M. RÜHLE, *J. Amer. Ceram. Soc.* **76** (1993) 426.
42. J. N. NESS, W. M. STOBBS and T. F. PAGE, *Phil. Mag.* A **54** (1986) 67.
43. O. L. KRIVANEK, T. M. SHAW and G. THOMAS, *J. Appl. Phys.* **50** (1979) 4223.
44. J. C. H. SPENCE, "Experimental High-Resolution Electron Microscopy", 2nd ed. (Oxford University Press, New York, 1988) p. 106.
45. R. F. EGERTON, "Electron Energy Loss Spectroscopy in the Electron Microscope", 2nd ed. (Plenum Press, New York, 1996).
46. L. REIMER, "Energy-Filtering Transmission Electron Microscopy" (Springer-Verlag Berlin Heidelberg, 1995) p. 347.

47. A. J. GUBBENS and O. L. KRIVANEK, *Ultramicroscopy* **51** (1993) 146.
48. A. BERGER, J. MAYER and H. KOHL, *ibid.* **55** (1994) 101.
49. F. HOFER, W. GROGGER, G. KOTHLEITNER and P. WARBICHLER, *ibid.* **67** (1997) 83.
50. Z. L. WANG, *ibid.* **67** (1997) 105.
51. H. BJÖRKLUND and L. K. L. FALK, *J. Eur. Ceram. Soc.* **17** (1997) 1301.
52. J. WASÉN, L. K. L. FALK and A. HJÖRNHEDE, "A Catalogue of Stereological Characteristics of Selected Solid Bodies, Vol. 2: Hexagonal Prisms" (Department of Engineering Metals, Chalmers University of Technology, Göteborg, 1996).
53. L. K. L. FALK and G. L. DUNLOP, *J. Mater. Sci.* **22** (1987) 4369.
54. D. P. THOMPSON, in "Silicon Nitride Ceramics: Scientific and Technological Advances," edited by I.-W. Chen, P. F. Becher, M. Mitomo, G. Petzow and T.-S. Yen (Materials Research Society, Pittsburgh, Pennsylvania, 1993) p. 79.
55. D. R. CLARKE and F. F. LANGE, *J. Amer. Ceram. Soc.* **63** (1980) 586.
56. O. J. PULLUM and M. H. LEWIS, *J. Eur. Ceram. Soc.* **16** (1996) 1271.
57. M. KNUTSON-WEDEL, "The Microstructure of Metal Oxide Additive Silicon Nitride Ceramics," Ph.D. thesis, ISBN 91-7197-280-3, Chalmers University of Technology, Göteborg, Sweden, 1996.
58. R. RAJ and F. F. LANGE, *Acta Metallurgica* **29** (1981) 1993.
59. H. KESSLER, H.-J. KLEEBE, R. W. CANNON and W. POMPE, *Acta Metall. Mater.* **40** (1992) 2233.
60. F. F. LANGE, L. K. L. FALK and B. I. DAVIES, *J. Mater. Res.* **2** (1987) 66.
61. Y. B. CHENG and D. P. THOMPSON, *J. Amer. Ceram. Soc.* **76** (1993) 76, 683.
62. D. J. GREEN, R. H. J. HANNINK and M. V. SWAIN, "Transformation Toughening of Ceramics" (CRC Press Inc., Florida, USA, 1989).
63. L. K. L. FALK, *Mater. Sci. Forum* **325/326** (2000) 231.
64. C.-M. WANG, X. PAN, M. J. HOFFMANN, R. M. CANNON and M. RÜHLE, *J. Amer. Ceram. Soc.* **79** (1996) 788.
65. H.-J. KLEEBE, M. K. CINIBULK, R. M. CANNON and M. R. RÜHLE, *ibid.* **76** (1993) 1969.
66. D. R. CLARKE, *ibid.* **70** (1987) 15.
67. D. R. CLARKE, T. M. SHAW, A. P. PHILIPSE and R. G. HORN, *ibid.* **76** (1993) 1201.

Received 6 June 2003
and accepted 20 January 2004